Forced Stage Response to a Moving Hurricane

JAMES F. PRICE

Woods Hole Oceanographic Institution, Woods Hole, Massachusetts

THOMAS B. SANFORD

Applied Physics Laboratory and School of Oceanography, University of Washington, Seattle, Washington

GEORGE Z. FORRISTALL

Shell Development Company, Houston, Texas

(Manuscript received 11 June 1992, in final form 5 January 1993)

ABSTRACT

The upper ocean's response to three hurricanes [Norbert (1984), Josephine (1984) and Gloria (1985)] is examined using field observations and a numerical ocean model. Our goal is to describe the physical processes that determine the structure and amplitude of hurricane-driven upper-ocean currents.

All three of these Northern Hemisphere hurricanes produced a rightward-biased response of the mixed-layer current and transport. This asymmetry arises because the wind stress vector rotates clockwise on the right side of the track and remains nearly parallel with the inertially rotating mixed-layer current during most of the hurricane passage. The maximum observed mixed-layer current varied from 0.8 m s^{-1} in response to Josephine, which was a large but comparatively weak hurricane, to 1.7 m s^{-1} in response to Gloria, which was very large and also intense.

These cases have been simulated with a three-dimensional numerical model that includes a treatment of wind-driven vertical mixing within the primitive equations. The simulations give a fairly good representation of the horizontal pattern and amplitude of the mixed-layer current, accounting for over 80% of the variance of the observed current. Model skill varies considerably with the amplitude of the mixed-layer current, being much higher for stronger currents than it is for weaker currents. This and other evidence suggest that a major contributor to the difference between the observed and simulated currents may be a noise component of the observed current that arises from measurement and analysis error and from prehurricane currents.

The Norbert case was distinguished by a large Burger number, $\sim 1/2$, which is a measure of pressure coupling between the forced stage mixed-layer currents and the relaxation stage thermocline currents. The observations and the simulation show upwelling of up to 25 m and strong thermocline-depth currents up to 0.3 m s^{-1} under the rear half of Norbert. Thermocline currents have a very simple vertical structure, a monotonic decay with increasing depth, and nearly constant direction. Their horizontal structure is more complex but appears to be due to an acceleration toward a low pressure anomaly associated with the first upwelling peak about 100 km behind the eye of Norbert.

1. Stages of the ocean's response

A moving hurricane is an intense and localized source of surface stress and stress curl whose passage excites several quite different modes of oceanic variability. To begin to sort these out, it is helpful to think of the ocean's response occurring in two stages. The "forced stage" response during the actual storm passage is a mainly local (depth and time dependent) response of the ocean to the very strong wind stress of the hurricane. The forced stage baroclinic response includes mixed-layer currents of O(1 m s^{-1}) (Sanford et al. 1987) and substantial cooling of the mixed layer and sea surface by vertical mixing (Black 1983; Stramma et al. 1986; Ginis and Dikiniov 1989). The barotropic response consists of a geostrophic current and an associated trough in sea surface height that are set up almost instantaneously (I. Ginis 1993, personal communication). Over a deep open ocean, the barotropic currents are comparatively small and do not interact strongly with the baroclinic response that we emphasize here. The time scale of the forced stage response is the storm residence time, which is typically half a day. The "relaxation stage" response following a hurricane passage is an inherently nonlocal (three-dimensional and time dependent) baroclinic response to the stress curl of the hurricane. The energy of the wind-driven mixed-layer currents is dispersed in a spreading wake of near-

Corresponding author address: Dr. James F. Price, Department of Physical Oceanography, Woods Hole Oceanographic Institution, Woods Hole, MA 02543.

inertial frequency internal waves (Geisler 1970; Gill 1984) that penetrate into the thermocline (Brooks 1983; Shay and Elsberry 1987; Brink 1989), eventually leaving behind a baroclinic geostrophic current along the storm track. The time scale of the relaxation stage response is typically 5–10 days [judged by the *e*-folding of mixed-layer currents, Price (1983) and Gill (1984)] and sufficiently long compared to the the forced stage response that there is generally little overlap of the dynamics (though we find some overlap in one case here).

In this paper we continue an analysis of the forced stage baroclinic response to three hurricanes that began with Sanford et al. (1987, hereafter S87). S87 described two field studies carried out in the fall of 1984 around Hurricane Norbert in the eastern North Pacific Ocean and Hurricane Josephine in the Sargasso Sea. We are able to include a third dataset acquired from a very similar field study carried out in the fall of 1985 with Hurricane Gloria, also in the Sargasso Sea. These three datasets are almost unique in showing the horizontal and vertical structure of the upper ocean's response to an intense storm, while also providing the means to estimate the two-dimensional and time-dependent field of wind stress that drives the response. Our plan is to

1) review the methodology and limitations of the field study (section 2a) and describe how we estimate surface stress from the measured winds (section 2b, which may be skipped by readers not interested in the issues of stress estimation);

2) introduce a new three-dimensional numerical model that will be used to simulate the ocean's response (section 3, which may be skipped by readers not interested in numerical models per se);

3) describe and interpret the structure of the forced stage response to include a test of the estimated wind stress (section 4a), and a test of the model's skill at simulating the mixed-layer current (section 4b);

4) describe some aspects of the thermal response (section 5);

5) examine how the mixed-layer currents begin to drive the relaxation stage response in the thermocline (section 6); and finally,

6) summarize the major results of this study and suggest how future studies might improve on the sampling and methodology introduced here and in S87 (section 7).

This study had a practical motivation in that hurricane-driven currents are a significant design parameter for offshore structures that might be subjected to hurricane conditions (Forristall et al. 1991). Major offshore structures are typically designed to withstand the maximum storm-driven currents (and surface gravity waves) that could be expected to occur during a life span of 100 years. If we can assume that the wind field of the 100-year storm is specified, then the maximum current has to be calculated using a numerical ocean model that is driven with the appropriate wind stress. To be most useful, the maximum current needs to be specified with an accuracy of about 0.2 m s^{-1} (which is a little better than we can do here). This requires that the wind stress estimation and the numerical model be verified by rigorous hindcasts of observed cases, which is one of the main objectives of this paper (section 4). To even approach the desired accuracy requires that the hindcasts be made as realistic as possible, and this has considerable impact on the way that we implement the numerical model.

The model simulations also have scientific utility in so far as they aid the interpretation of the field data. In particular, the continuous model fields help to reveal the large-scale pattern underlying the somewhat sparse AXCP (air-deployed expendable current profiler) observations. They also help by showing the kinematic and dynamic relationships among variables—the forced stage mixed-layer current and the relaxation stage thermocline current—that would be very hard to infer from the field data alone.

2. Review of the field experiment and data analysis

Oceanographic and meteorological measurements were made by a National Oceanic and Atmospheric Administration (NOAA) P3 aircraft that flew a star-shaped flight path *once* through each hurricane. (Figure 1 shows the flight path through Gloria, and the other two cases are shown in S87.)

a. Oceanographic data

The aircraft dropped AXCPs at roughly 40-km intervals along the flight path. In each case there were about 15 AXCPs that produced usable data. (Figure 2 shows the hurricane tracks and the AXCP locations, and Table A1 of the Appendix lists station data for each AXCP.) AXCPs measure ocean temperature much like a conventional XBT, and they also sense the motionally induced electric field set up by ocean currents and surface gravity waves. To separate the surface waves from the ocean currents, S87 fit the AXCP data to a model having a surface wave component and a three-layer linearly varying current profile (the details are in the Appendix, which includes a listing of the Gloria data in Table A2). S87 estimated that the precision in the resulting fitted currents (due to measurement error, due to specification of the reference level current for each profile, and due to misfit of the three-layer model including the separation of the surface gravity wave component) was 0.2 m s^{-1} rms. In this study we identify an additional error source associated with prehurricane currents (more on this below).

1) THE OCEAN INITIAL CONDITION

These datasets are one-time views of ocean temperature and currents beneath the moving hurricanes; they

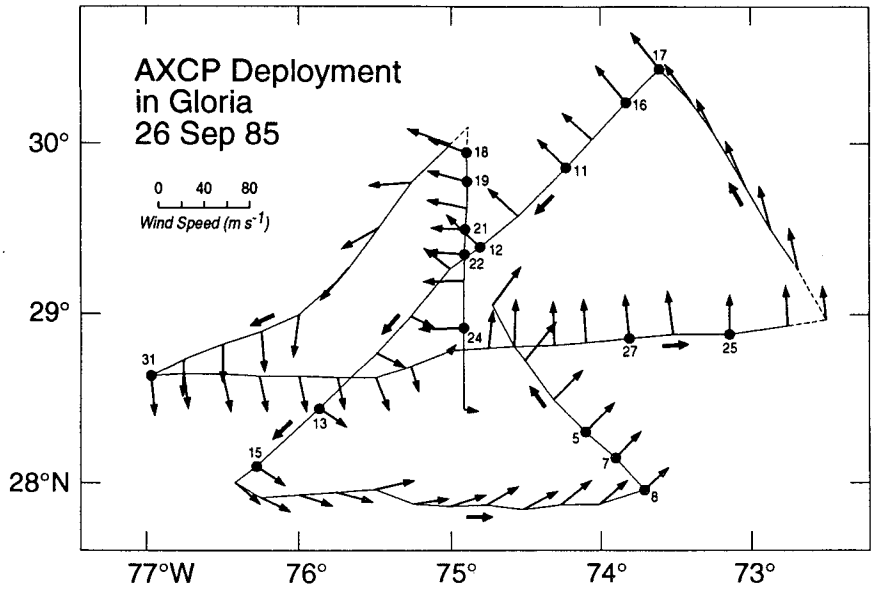

FIG. 1. Flight path through Hurricane Gloria. Wind vectors are shown at roughly 35-km intervals along the flight path; AXCP positions are the numbered dots along the path. Hurricane Gloria was moving to the northwest during the time of the survey.

do not include the prehurricane survey data required to define the ocean initial condition. (We chose to use the available resources to survey once in each of three different cases rather than twice or three times in one case.) In the absence of prehurricane data we necessarily make the following two approximations, or simplifications, regarding the ocean initial condition.

1) In both the data analysis and in the simulations we assume that the initial ocean is horizontally homogeneous. The initial temperature profile is taken from AXCP temperature profiles made under the leading edge of the hurricanes (Fig. 3: Norbert AXCP N2; Josephine AXCPs J20 and J21; Gloria AXCPs G31 and G18).

The homogeneity assumption is violated to some degree in the Sargasso Sea cases. As noted in S87 and in Black et al. (1988), satellite imagery of the survey areas (National Weather Service/National Environmental Satellite Service Oceanographic Analysis) reveals prehurricane SST variability of several degrees centigrade associated with the subtropical frontal zone (Voorhis 1969). The AXCP data also show evidence of prehurricane variability in that the coolest sea surface temperatures and some of the largest thermocline currents O(0.2 m s^{-1}) are found under the leading edge of Josephine and Gloria (i.e., toward the north), which we believe cannot be due to the hurricane response. Because this prehurricane variability is as large as the expected ocean response of SST and thermocline currents, the interpretation of those specific ocean data is problematic and is not discussed here in detail. (We show the Gloria SST data in section 5a.) The Norbert dataset exhibits much less prehurricane variability and is emphasized when we discuss the SST and thermocline response.

2) In the data analysis we assume that prehurricane upper-ocean currents can be treated as a random noise that is superimposed on the hurricane response (amplitude estimated below). In the model simulations we assume that the initial currents were zero. This latter assumption could introduce an error in the dynamics of the model if the horizontal shear of the prehurricane currents was comparable to the Coriolis parameter, f (Klein and Hua 1988), or if the vertical shear of those currents was comparable to the wind-driven current shear. The available AXCP data are not sufficient to resolve the prehurricane currents in enough detail to include them as a deterministic feature, and we necessarily neglect this interesting possibility.

2) NOISE LEVEL ON THE OBSERVED UPPER-OCEAN CURRENTS

The amplitude of the prehurricane currents in the Sargasso Sea cases may be estimated from two sources. Black et al. (1988) describe drifter tracks from the Josephine survey region that show a complex pattern of low-frequency currents associated with the subtropical front and a superimposed near-inertial current that is part of the response to Josephine. The low-frequency currents had an amplitude of 0.2 m s^{-1} rms. As noted above, we found that the upper-thermocline currents observed under the forward edge of Josephine and Gloria were about 0.2 m s^{-1} rms (they were consid-

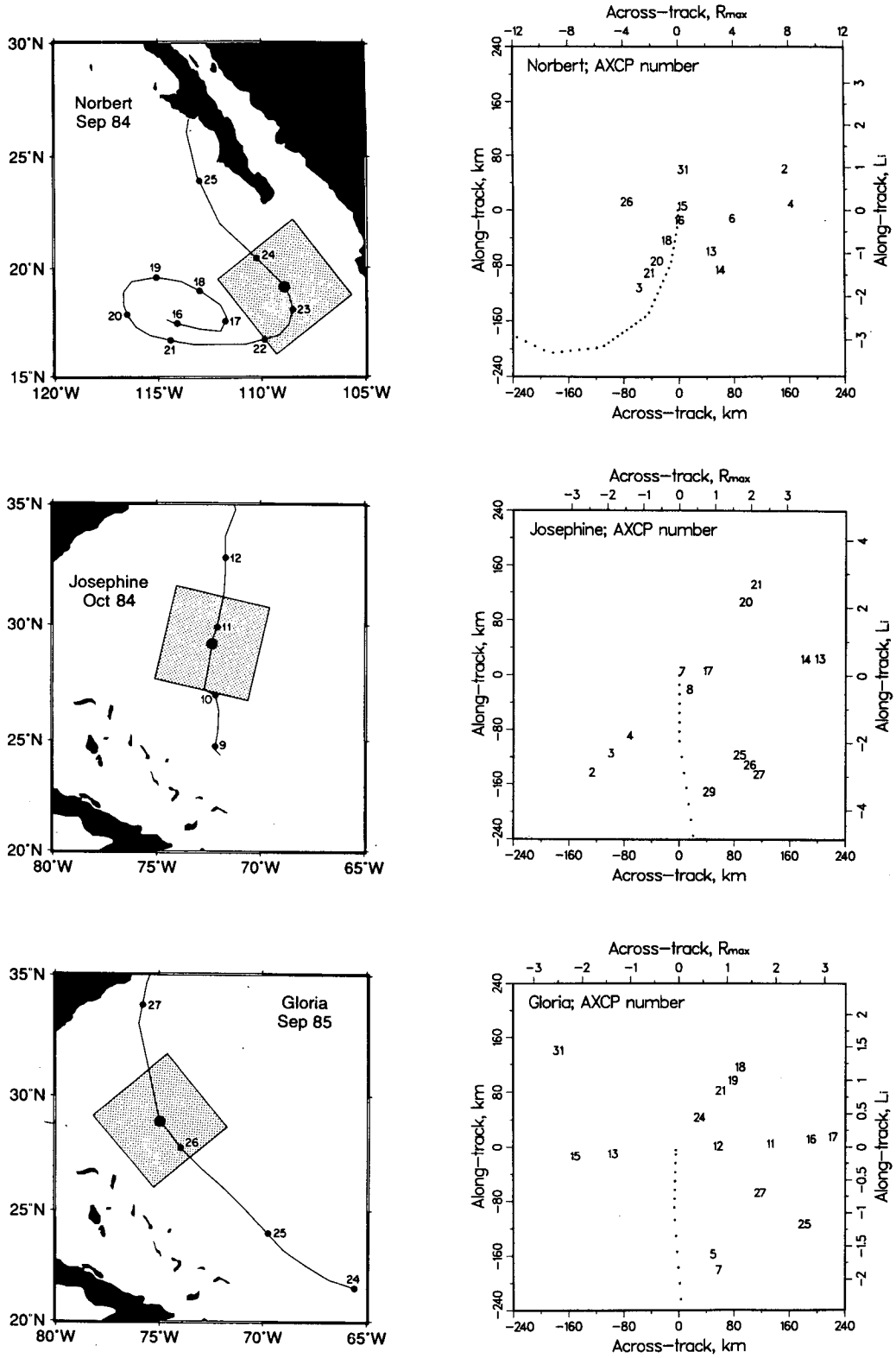

FIG. 2. (left side) Hurricane tracks and survey regions (shaded) of from top to bottom: Norbert, Josephine, and Gloria. Date is shown at 0000 UTC along the tracks. (right side) AXCP positions shown in a storm-centered coordinate system (described in section 2c) that is defined for the period of the surveys. In this system the hurricanes are translating due north along their respective tracks (shown as a dotted line at 1-h intervals) as they reach the origin.

erably smaller under Norbert), which we therefore take as the amplitude of prehurricane currents.

Recall that S87 estimated that the measurement and analysis precision on a fitted AXCP current component was also about 0.2 m s^{-1} rms. From this we estimate that the net uncertainty (precision and accuracy) of interpreting an observed, fitted current estimate as if it were strictly a hurricane-driven current is $V_{noise} = \sqrt{0.2^2 + 0.2^2} \approx 0.3$ m s^{-1} rms.

The saving feature for this study is that the *largest* hurricane-driven mixed-layer currents are O(1 m s^{-1}) and stand well above this V_{noise}. Thus, the horizontal pattern of the mixed-layer current is clear in all three of the datasets, and for example, there is a significant variation in current amplitude between the three cases that can be readily interpreted as a consequence of hurricane size and intensity. However, the hurricane response is strongly inhomogeneous spatially. In those regions where the hurricane response is small (it can nearly vanish on the left side of the track, for example) we can expect that V_{noise} may completely obscure the hurricane response, especially in the two Sargasso Sea cases.

b. *Meteorological data*

An important step in this study is to estimate the two-dimensional and time-dependent field of surface wind stress due to the moving hurricanes. We do this by the simplest and most direct method allowed by the available meteorological data.

Wind and pressure measurements were made by the NOAA P3 aircraft at a flight level that varied considerably between the three cases. Flight level was 1500 m in Norbert, 500 m in Josephine, and considerably higher in Gloria, 3300 m, because of severe turbulence. Because the Norbert and Josephine data were taken within the planetary boundary layer we can attempt to estimate surface layer winds from a simple extrapolation procedure. This would not be appropriate in the Gloria case where instead we use the results from a simulation of the hurricane planetary boundary layer.

1) STRESS ESTIMATION FOR NORBERT AND JOSEPHINE

Flight-level winds were subsampled to provide a wind vector at roughly 10-km intervals along each of the radial sections flown through the hurricanes (Fig. 1 and Fig. 11 of S87). These subsamples were taken when the aircraft was in a more or less steady attitude to minimize measurement errors. To calculate surface stress we must then extrapolate the flight-level winds to a standard height near the surface, 10 m. This extrapolation is done by a reduction of amplitude estimated from an empirical (Bates) profile given by Powell (1980) and by a rotation of the wind vector toward lower pressure estimated from Frank's (1977) analysis. Because flight level was somewhat higher in Norbert, the amplitude reduction and rotation are both slightly larger than for Josephine, Table 1. The uncertainty in the amplitude reduction was estimated from the error bars on the original figures of Powell (1980).

These estimated 10-m winds then have to be analyzed onto a regular grid before they can be used in the simulation model. To do this we have chosen to fit these data to a model hurricane (rather than interpolate onto a grid) because the front left half of Josephine was not sampled and also because a fitting procedure yields a much more portable result for other investigators. The form of the model hurricane was taken to be the composite hurricane compiled by NOAA/NWS (1979) for use in design studies. This model hurricane is specified by a radial profile of wind speed and inflow angle (the angle between the wind and the azimuthal direction; positive angle indicates that the wind blows toward the hurricane center) listed in Table 1. The radius is normalized by the radius to maximum wind speed, R_{max}, and wind speed is nor-

TABLE 1. Wind analysis and hurricane model fitting.

Extrapolation to 10-m height

	Norbert	Josephine
Nominal flight level (m)	1500	500
Amplitude reduction (%)	33 ± 7	27 ± 7
Rotation (deg)	16	10

Model hurricane radial profiles

Radius/R_{max}	Wind speed/U_{max}	Inflow angle (deg)
0.0	0.0	0
0.4	0.1	2
0.7	0.5	4
0.8	0.8	6
0.95	0.95	7
1.0	1.0	7
1.35	0.97	14
2.7	0.72	23
4.05	0.54	24
5.4	0.44	22
6.75	0.4	21
8.1	0.36	21
10.8	0.27	21
13.5	0.23	21
27.0	0.0	20

Best fit parameters

	Norbert	Josephine	Gloria
Radius to maximum wind, R_{max} (km)	20 ± 2	52 ± 3	70 ± 5
Maximum wind speed, U_{max} (m s^{-1})	36 ± 2	29 ± 2	36 ± 3
Percent variance accounted for	93	94	96
Rms error of the fit (m s^{-1})	6	6	0.010[a]

[a] Gloria was fit on U_*, not wind speed as were Norbert and Josephine.

malized by the maximum wind speed, U_{max} (dimensional values for each case are given herein).

Translation of a hurricane will induce an asymmetry of wind speed, with larger values occurring on the right side of the track where the cyclonic winds and the hurricane translation add constructively. To include this asymmetry we add on an additional vector wind $\mathbf{U}_H/2$, consistent with the recommendations of NOAA/NWS (1979).

The model hurricane (including the asymmetry noted above) was fitted to the 10-m winds by varying R_{max} and U_{max} to minimize the mean-square difference between the observed winds and the model hurricane winds. The best fit R_{max} and U_{max} for each hurricane are listed in Table 1 along with the percent variance accounted for by the best fit model and the rms wind velocity that could not be accounted for by the best fit. In both cases the percent variance accounted for was in excess of 90%, suggesting that the NOAA/NWS (1979) model hurricane is appropriate for Norbert and Josephine. Visual comparison of the observed and fitted winds gives the same impression. While there are, of course, mesoscale variations of the observed wind that are not included in the model hurricane, these are small compared to the largest winds and do not have a systematic, hurricane-scale pattern.

The surface stress, $\boldsymbol{\tau}$, was calculated from the model 10-m wind vector, $\mathbf{U}_{10}$, using the usual bulk transfer formula,

$$\boldsymbol{\tau} = \rho_a C_d U_{10} \mathbf{U}_{10}, \tag{1}$$

where ρ_a is the density of air and U_{10} is the 10-m wind speed. The drag coefficient C_d is the Large and Pond (1981) neutral form:

$$C_d = 1.14 \times 10^{-3} \text{ if } U_{10} < 10 \text{ m s}^{-1} \tag{2}$$

or

$$C_d = (0.49 + 0.065U_{10}) \times 10^{-3} \text{ if } U_{10} > 10 \text{ m s}^{-1}. \tag{3}$$

This C_d is very similar to that inferred from hurricane wind observations using the ageostrophic method by Miller (1964) (and see also Powell 1980).

Both Norbert and Josephine moved along rather complicated tracks (Fig. 2) that were observed by aircraft and satellite reconnaissance. These tracks are an important part of the simulations, as we will discuss further in section 3c.

2) Stress estimation for Gloria

Because the flight level in Gloria was at 3300 m and above the planetary boundary layer, we have not applied the simple extrapolation and model fitting procedure described above. Instead, the Gloria stress field was estimated for this project by V. J. Cardone of Oceanweather, Inc. using a numerical model of the planetary boundary layer below a translating, atmospheric vortex (Cardone et al. 1980). The time-dependent pressure field of the vortex and the synoptic-scale environment were specified from observations, and the Oceanweather model then computed the surface friction velocity by means of a similarity theory of the marine boundary layer. This gave the stress field at 30-min intervals over the survey region.

To compare this result with that from the simple extrapolation method, we have also had the Norbert and Josephine pressure datasets run through the Oceanweather analysis. This showed that the Oceanweather stress fields were very similar to those estimated from our extrapolation procedure. The maximum stress occurred at slightly larger radius (by about 10%–15%), but the maximum stress was almost identical, as was the overall storm size. The end result was that the ocean model gave virtually the same simulation when driven with either of the wind stress fields described above. On that basis, we presume that the Gloria wind stress fields are equivalent to those from the analysis of Norbert and Josephine. (See also validation tests by Cardone and Ross 1979; Cardone et al. 1980; Forristall et al. 1977; Forristall et al. 1978.)

To compare this hurricane with Norbert and Josephine, we have fit the model-estimated friction velocity to the friction velocity of our simple hurricane wind profile model. The best fit gave $R_{max} = 70$ km and $U_{max} = 36$ m s^{-1}. Compared with the other two hurricanes, Gloria was a very large and powerful storm (Fig. 3).

3) Comments on the wind stress

The wind stress estimated by either of the methods described above is, at best, an estimate of the stress within the planetary boundary layer. To simulate ocean currents we need to know the stress at the top of the ocean surface mixed layer. Under quasi-steady conditions, surface gravity waves appear to be a nearly transparent intermediary in the momentum transfer from the wind to the surface current (Stewart 1974), and these two stresses will be essentially the same. Under hurricane conditions, surface waves are presumably quite nonstationary, and their growth or decay could possibly lead to a nonlocal momentum transfer from the planetary boundary layer to ocean currents. Thus, it is not obvious a priori that these wind stress estimates will be an accurate measure of the stress within the ocean surface mixed layer. A contribution of this work is that we can test the estimated wind stress by comparing the simulated transport with the observed transport calculated from the AXCP field data (section 4a).

c. Storm-centered coordinate system

The AXCP data were taken along radial sections that were flown through the eyes of the moving hur-

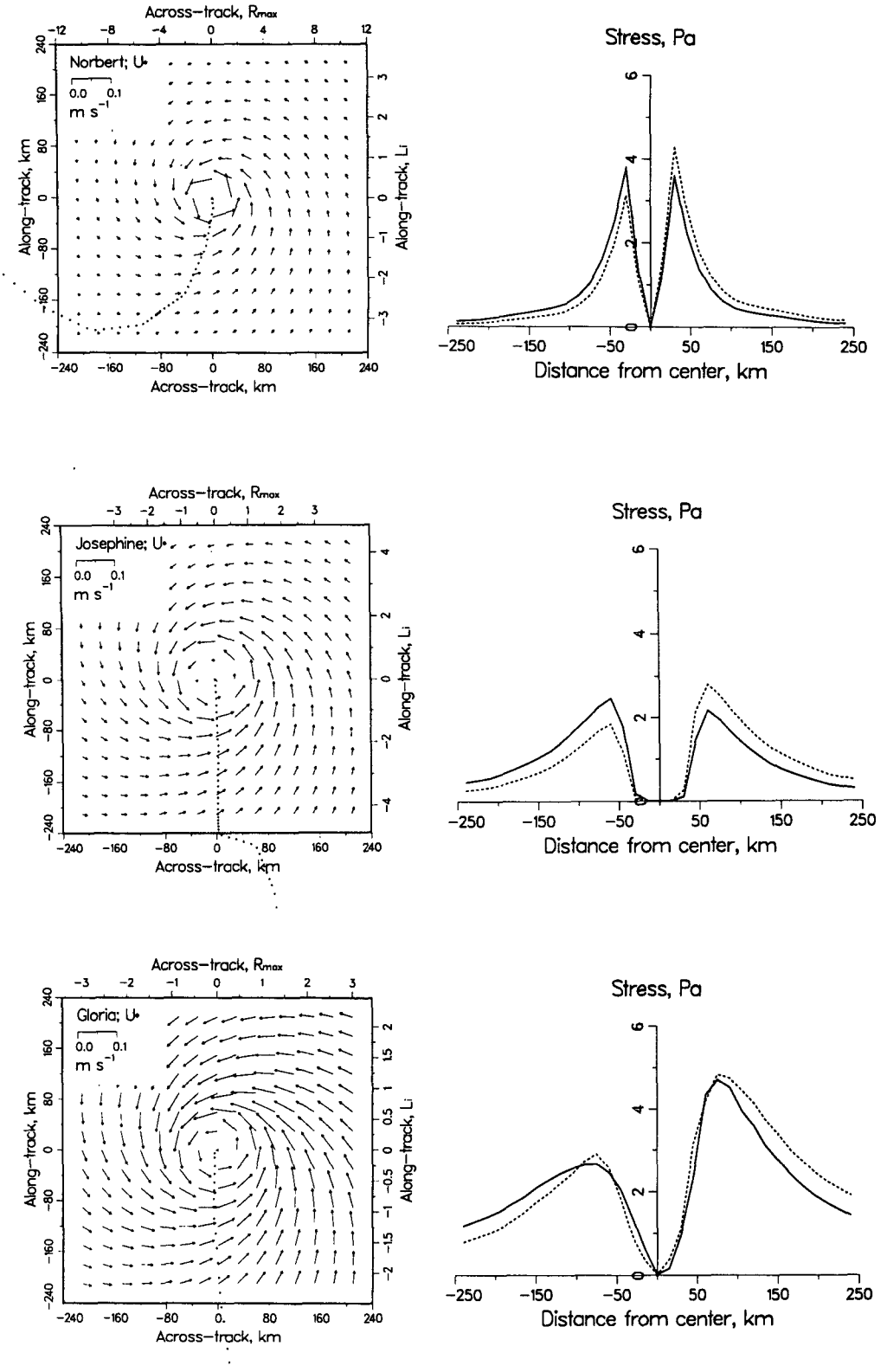

FIG. 3. (left side) Wind stress for Hurricanes Norbert, Josephine, and Gloria shown as friction velocity in plan view. (right side) Wind stress amplitude shown in cross sections through the hurricanes; the solid line is a slice along the track; the dashed line is a slice made across the track.

ricanes. Each flight required about four hours, during which the hurricanes moved about 100 km (Gloria) or about 50 km (Norbert and Josephine). To show the ocean response in relationship to the hurricane forcing and to provide a quasi-synoptic view of the response, we have analyzed the data in a storm-centered coordinate system that is defined for the period of the surveys. Thus, an AXCP drop made at time $t_d = t_c + \Delta t$ and at a geographic position $\mathbf{X}_d = \mathbf{X}_c + \Delta\mathbf{X}$ would have a storm-centered coordinate $\mathbf{X} = \mathbf{X}_d - \mathbf{X}_c - \Delta t\mathbf{U}_H$, where $\mathbf{X}_c$ is the hurricane eye position at the central time of the survey, t_c, and again, $\mathbf{U}_H$ is the average (vector) translation speed of the hurricane during the time of the surveys (Table 2). The maximum shift required to place an AXCP in this coordinate system is about 50 km for AXCPs dropped at the beginning or end of the Gloria survey and about half as much for the other two cases. Given possible errors in the reported hurricane tracks (which are minimized since the aircraft that made the AXCP drops also provided much of the tracking data) and possible variations in the translation speed or direction, we estimate that the error in placing an AXCP in the storm-centered coordinate system is approximately 20 km rms for positions that are farthest from the eye and less, approximately 5 km rms, for those within 50 km of the eye. This is not a major contributor to error in the overall analysis.

To facilitate a comparison of the three cases the storm-centered coordinate system is rotated so that $\mathbf{U}_H$ at the time of the surveys is directly up the page (northward) in plan view diagrams. A compilation of current data in this coordinate system is in Table A3.

This storm-centered coordinate system is defined locally in time around the comparatively short period of the flights, and it cannot account for changes in hurricane speed or direction that occurred before the time of the surveys. For example, Norbert comes into the survey region from the "west," when viewed from the storm center coordinate system (Fig. 2, upper right) but is moving due "north" as it arrives at the center of the survey region.

3. Numerical simulation model

The numerical simulations are made with a three-dimensional, primitive equation, hydrostatic model that represents vertical structure on a fixed grid.

a. Model approximations and equations

The temperature, salinity, and momentum budgets are the usual:

$$\frac{\partial T}{\partial t} + \mathbf{V}\cdot\nabla T + W\frac{\partial T}{\partial z} = \frac{1}{\rho_0 C_P}\frac{\partial H}{\partial z} \tag{4}$$

$$\frac{\partial S}{\partial t} + \mathbf{V}\cdot\nabla S + W\frac{\partial S}{\partial z} = \frac{\partial E}{\partial z} \tag{5}$$

$$\frac{\partial \mathbf{V}}{\partial t} + f\mathbf{k}\times\mathbf{V} + \mathbf{V}\cdot\nabla\mathbf{V} + W\frac{\partial \mathbf{V}}{\partial z} = \frac{1}{\rho_0}\frac{\partial \tau}{\partial z} - \frac{1}{\rho_0}\nabla P, \tag{6}$$

where $\mathbf{V}$ and ∇ are the horizontal current and gradient operator and W is the vertical component of the velocity computed by integrating the continuity equation from the surface downward:

$$W(z) = \int_0^z \nabla\cdot\mathbf{V}\,dz. \tag{7}$$

Here H, E, and τ are the heat, salt, and momentum (vertical) fluxes whose surface values are prescribed from air–sea exchange formulas; their vertical distribution is determined implicitly by the mixing parameterization described below. The surface value of the momentum flux, $\tau(0)$, was discussed in detail in section 2b. The surface heat flux, $H(0)$, is computed assuming an air temperature that is 3°C less than the initial sea surface temperature and a dewpoint temperature that is 4°C less (e.g., Malkus 1962), and using a bulk transfer coefficient of 1.3×10^{-3} for sensible and latent heat flux. This gives an air–sea heat flux of up to 600 W m^{-2}, which is small compared to the heat flux due to vertical mixing (Price 1981; Greatbatch 1985). The salt flux at the surface is taken to be zero, $E(0) = 0$, in the absence of data on salinity or precipitation. A climatological salinity profile is included in the ocean initial condition.

The Coriolis parameter f is assumed to be uniform. This is acceptable for a few days after the hurricane passage or before the inertial wave wake has had time to disperse horizontally away from the track (Geisler 1970).

The hydrostatic pressure perturbation P is computed assuming that the abyssal ocean is infinitely deep (reduced gravity approximation), which excludes the dynamics of fast barotropic waves. This is appropriate for the deep, open ocean study sites considered here where the abyssal current response is expected to be very small, O(0.02 m s^{-1}), compared to the wind-driven current in the mixed layer, which is O(1 m s^{-1}) (Geisler 1970). [For a discussion of the barotropic response, see Cooper and Thompson (1989a, 1989b).] Under this approximation the perturbation pressure becomes

$$P(z) = -g\int_{z_a}^{z} (\rho(z) - \rho_0(z))dz, \tag{8}$$

where g is the acceleration of gravity. Vertical integration is started at the top of the abyssal ocean, $z_a = 1000$ m, where $P = 0$ under the reduced gravity approximation. The perturbation density is computed from a linear state equation:

$$\rho(z) - \rho_0(z) = \alpha(T - T_0) + \beta(S - S_0), \tag{9}$$

where T_0 and S_0 are the initial temperature and salinity, and α and β are the thermal and haline expansion coefficients, all of which are depth dependent.

The only subgrid-scale process recognized in the model is upper-ocean vertical mixing, which is an important process in the forced stage response (Chang and Anthes 1978; Martin 1982). In this model vertical mixing is treated by the hybrid mixed-layer formulation of Price et al. (1986), which assumes that the upper-ocean density and velocity will be mixed vertically to satisfy three stability criteria that require (with z positive upward)

$$-\frac{\partial \rho}{\partial z} \geq 0 \quad \text{for static stability} \quad (10)$$

$$R_b = \frac{-g\delta\rho h}{\rho_0(\delta \mathbf{V})^2} \geq 0.65$$

for mixed-layer shear flow stability (11)

and

$$R_g = \frac{-g\partial\rho/\partial z}{\rho_0(\partial \mathbf{V}/\partial z)^2} \geq \frac{1}{4}$$

for stratified shear flow stability. (12)

[The δ operator in (11) takes the vertical difference across the base of a mixed layer that is developed during a time step; see Price et al. (1986) for details.] This parameterization has been tested extensively and compared to other mixed-layer formulations by Martin (1986) and Archer (1990). Two key features for this study are that this parameterization gives significant vertical mixing where R_b is reduced below 1, which in practice occurs where the mixed-layer current is strongly accelerated by the wind stress. We can check this for consistency by examining bulk Richardson numbers estimated from AXCP data (section 5c). Second, the shear flow stability criterion produces vertical mixing in a transition layer below the surface mixed layer when there is sufficient vertical shear to reduce the gradient Richardson number below 1/4. This too can be checked for consistency with the field observations.

b. Implementation

To resolve the transition layer it is necessary that the model have a vertical grid spacing of 10 m within the upper 150 m where vertical mixing might occur. The resolution requirements are otherwise much less severe, and the grid spacing increases to 50 m and then to 100 m for greater depths down to the base of the thermocline, 1000 m. The model has 25 grid levels.

Horizontal structure is represented on a regular grid having resolution of 15 km. Spatial differencing is done with a simple second-order scheme in both the vertical and horizontal. The model was integrated with a time step of 1800 s using the three time level, leapfrog-trapezoidal method. We have tried increasing the horizontal resolution and the temporal resolution by a factor of 3, separately and together, and find that the solutions are remarkably insensitive to these changes. There is no need for a horizontal diffusion process since the duration of the integrations is very short compared to the growth rate of small-scale numerical instabilities.

A simple radiation boundary condition using a phase speed of 2 m s^{-1} was applied on the sides of the model grid to simulate an open ocean domain. Changes in the width of the model domain were found to cause no change whatever in the central portion of the domain that represents the survey areas, suggesting that boundary artifacts are negligible.

c. Model tuning or model development?

This model has no free or adjustable constants, and the solutions have not been adjusted in the usual sense of parameter tuning. However, the *model itself* has evolved in two major steps during the course of this project. In each case the model changes were indicated by a comparison of preliminary model results with the field data. Hence, these model changes could be regarded as model tuning on a large scale, or they could be regarded as model development. In either case, they represent a part of what we have learned about simulating real datasets, and we recount them briefly.

The first change dealt with the hurricane's motion. At the outset we began with the Price (1981) model, which assumed that the hurricane moved along a straight course at constant speed. We found that the simulated currents from this model showed systematic phase errors (when compared with the AXCP data), which we suspected might arise because the actual hurricanes moved along curving tracks and at variable speeds. Model experiments confirmed this, showing that course or speed changes may be important if they cause a change in stress direction (as seen from the ocean) of more than about 30 deg or, equivalently, if they cause a change in hurricane residence time of more than about two hours (see also Cooper and Thompson 1989a). To simulate these cases at the level of detail required here, it was therefore necessary to translate the model hurricanes over the observed tracks (Fig. 2). The model integrations were begun at a time when the hurricanes were well outside the survey regions. The hurricanes were moved along the observed tracks and at the observed translation speeds until the hurricanes reached the central positions of the surveys, $\mathbf{X}_c$, given in Table 2. The integration was then stopped and the solutions saved for later analysis. While this rather complicated procedure may be appropriate for our purpose here, we should note that for the purpose of demonstrating and understanding most physical processes of the response one could just as well utilize a steadily translating storm as have Greatbatch (1983) and Shay et al. (1989), among others.

TABLE 2. Central position and speed of the hurricanes.

	Norbert	Josephine	Gloria
Time (UTC) and date	0112 24 Sep	0941 11 Oct	0700 26 Sep
Position	19.41°N, 109.08°W	29.41°N, 72.13°W	28.75°N, 74.98°W
Translation speed, U_H (m s^{-1})	3.2 ± 0.5	3.5 ± 0.2	6.8 ± 1.0
Course (deg T)	320 ± 5	10 ± 5	325 ± 5

The second change dealt with the representation of vertical wind mixing. The Price (1981) model employed a conventional mixed-layer formulation that confined all wind mixing to a surface mixed layer and thus developed a sharp jump in density and current across the base of that layer. Observed density and current profiles (an example is in the Appendix and in later figures) seldom show such sharp jumps; instead, they show a continuous and smooth (at the several meter scale) variation of density and current across the base of the mixed layer. This variation occurs over a so-called transition layer whose thickness may be comparable to that of the mixed layer. A direct comparison of observed profiles with those from a conventional mixed-layer model may thus require considerable interpretation of the model results. For example, we found that the mixed-layer depth simulated by the Price (1981) model was consistently deeper than the observed mixed-layer depth, even though the mixed-layer cooling and mixed-layer currents had a plausible amplitude (Price et al. 1991). To avoid having to deal with this kind of inherent model failure, we eventually dropped the conventional mixed-layer formulation and adopted the hybrid (grid-level) mixed-layer formulation of Price et al. (1986) that admits the possibility of mixing below the mixed layer [as does the turbulence closure model of Mellor and Yamada (1982), among others]. The simulations of current and density profiles from this model can be compared with field data in a straightforward way. Again, while this is useful for the present purpose, it may not be needed for many other purposes, for example, simulations of SST cooling (Greatbatch 1985) or modeling the horizontal structure of the response, for which a conventional mixed-layer model would give an equivalent result.

d. Nondimensionalization and scaling

The external parameters that characterize the ocean and a steadily translating hurricane are defined and listed in Table 3 (note that we do not attempt to deal with track curvature). The external parameters that change the most from case to case are those that characterize the hurricanes. For example, R_{max} varied from 20 km for Norbert to 70 km for Gloria, and the translation speed also varied by at least a factor of 2. The form of the nondimensionalization for the independent variables (i.e., coordinates) and for the dependent variables (e.g., the mixed layer current) is that appropriate for a large and fast moving storm, and was developed by Geisler (1970), Price (1983), and Greatbatch (1984). The form for the thermocline current is developed in section 6b. We refer to these nondimensional variables only sparingly and emphasize dimensional quantities throughout.

The external parameters can be grouped into five nondimensional parameters whose values can give us a qualitative idea of the character of the ocean response:

1) The nondimensional storm speed, S, which is the ratio of the local inertial period to the hurricane residence time. In each case, S is O(1), so that the wind stress seen from the ocean changes on a time scale comparable to the local inertial period. As a consequence, we would expect that the response of upper-ocean currents will include strong inertial motions and will be asymmetric across the track (sections 4a and 4b).

2) A Burger number, B, which is a direct measure of the pressure coupling between the mixed-layer current and the thermocline current (this is shown in section 6c). Given the fairly large Burger number in the Norbert case, we would expect that pressure coupling and the relaxation stage dynamics would be most pronounced in that case.

3) A Mach number, C, which is the ratio of storm translation speed to the gravest mode internal wave phase speed, here taken to have a nominal value $c = 2$ m s^{-1}. Geisler (1970) and Greatbatch (1984) showed that when a storm moves at a speed only slightly greater than c, the response will include significant upwelling directly beneath the storm and will include a substantial geostrophic component.

4) A Rossby number for the mixed-layer current, Q, which is the ratio of horizontal advection of momentum to the Coriolis force. The small size of Norbert would be expected to lead to enhanced nonlocal effects by horizontal advection during the forced stage response (we do not pursue this).

5) The aspect ratio of the mixed-layer thickness to the thermocline thickness, b, is A, which is important in the relaxation stage response at long times (nor do we pursue this).

4. The forced stage response of upper-ocean currents

a. Upper-ocean transport

We begin with a discussion of the upper-ocean transport (rather than the current) in order to make a

TABLE 3. Scaling.

	Norbert	Josephine	Gloria
External parameters			
U_H (m s^{-1})	3.0	3.5	6.8
R_{max} (km)	20	52	70
τ, Pa (*a*)	4.0	2.5	4.0
f, s^{-1}	4.8×10^{-5}	7.1×10^{-5}	7.0×10^{-5}
$g' = \frac{g\Delta\rho}{\rho_0}$, m s^{-2} (*b*)	0.04	0.04	0.04
h_1, m (*c*)	40	60	50
b, m	350	500	500
Scales for the independent variables			
Across-track scale = R_{max}, km	20	52	70
Alongtrack scale $L_i = \frac{U_H}{f}$, km	62.5	49.3	97.1
Time scale = $\frac{2\pi}{f}$, s	1.30×10^5	8.85×10^4	8.97×10^4
Depth scale in the thermocline = b, m	350	500	500
Scales for the dependent variables			
$\tilde{U}_{ml} = \frac{2\pi R_{max}}{\rho_0 h_1 U_H}$, m s^{-1}	1.30	1.20	1.60
$\tilde{\eta} = \frac{\tau}{\rho_0 f U_h}$, m	27	10	8
$\tilde{P} = \frac{g'\tau}{fU_H}$, Pa	1100	400	320
$\tilde{U}_{tcl} = \frac{g'\tau}{\rho_0 f U_H^2}$, m s^{-1}	0.36	0.11	0.05
Nondimensional variables			
$S = \frac{\pi U_H}{4fR_{max}}$	2.4	0.8	1.1
$B = \frac{g'h_1}{4f^2R_{max}^2}$ (*e*)	0.37	0.04	0.02
$Q = \frac{\tau}{\rho_0 h_1 U_H f}$	0.7	0.2	0.2
$C = \frac{U_H}{c}$	1.5	1.7	3.4
$A = \frac{h_1}{b}$	0.15	0.10	0.10

(*a*) An average of the maximum values on the left and right sides of the hurricane.
(*b*) The density change across the thermocline is $\Delta\rho = 4$ kg m^{-3}.
(*c*) Depth of the top of the seasonal thermocline.

consistency check on the estimated wind stress. A useful check is possible because the simulated transport is proportional to the wind stress amplitude and is almost independent of the model-specific parameterization of vertical mixing. The simulated transport is affected somewhat by the pressure coupling between the mixed layer and the thermocline. However, this is a well-resolved process (in a computational sense) and is not model dependent.

The transport (volume transport per unit width) is estimated from the AXCP data using the fitted current components and from the model solutions as

$$\mathbf{M} = \int_{-80}^{0} \mathbf{V} dz,$$

where the lower limit of integration has been chosen to be slightly deeper than the transition layer at most AXCPs. Starting the integration at a somewhat deeper level, $z = -100$ m, which is equally plausible, gives nearly identical results. The observed and simulated transport vectors are plotted in Figs. 4a, 5a, and 6a) in the so-called storm-centered coordinate system. The axes on these plots show distance in dimensional units, which are held constant among the three cases, and also in nondimensional units (section 3d and Table 3) at top and on the right. These latter scales change from one case to the next.

1) THE COUPLING BETWEEN WIND STRESS AND UPPER-OCEAN TRANSPORT

The dominant pattern in each case includes a very pronounced rightward bias in the amplitude (noted also in S87 and by Church et al. 1989). For example, at a position 100 km to the right and behind the center of Gloria (Fig. 6a) the observed transport is about 120 m^2 s^{-1}, while at the same distance to the left of the track the amplitude is only about 25 m^2 s^{-1}. A comparable rightward bias occurs in the model solutions because of an inherent asymmetry in the coupling between the wind stress of a moving hurricane and the upper-ocean transport. The transport (and the current) tends to rotate inertially (clockwise in this Northern Hemisphere case) since pressure gradient forces are generally small compared to the Coriolis force (Greatbatch 1983). On the right side of the track the wind stress also turns clockwise with time when viewed from the ocean. When the nondimensional storm speed S is O(1), as it is here and for most hurricanes, the wind stress rotation rate roughly matches the inertial rotation rate of the transport (Chang and Anthes 1978; Price 1981), and the end result is that the transport and wind stress remain roughly aligned throughout most of the hurricane passage.

On the left side of the track the coupling between the transport and the wind stress is much less efficient because the wind stress rotates anticlockwise during the hurricane passage. Under the leading edge of the hurricane the wind stress begins to accelerate the resting ocean but within about four hours the tendency for clockwise rotation of the transport combined with the anticlockwise rotation of wind stress cause the transport and wind stress to be roughly antiparallel during most of the hurricane passage. The result is that the transport never becomes very large on the left side of the track.

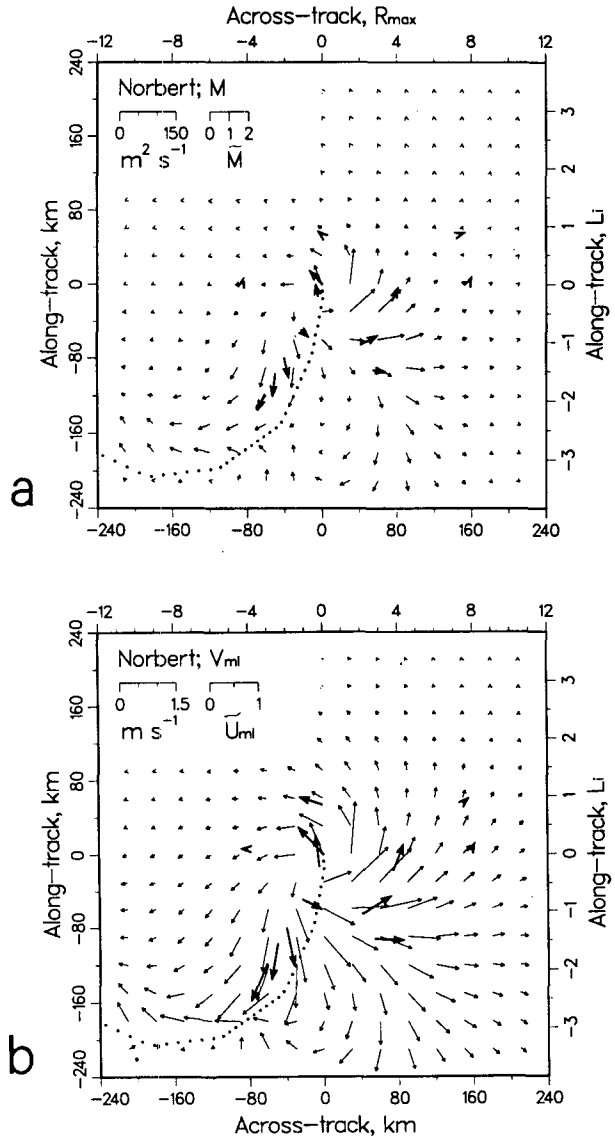

FIG. 4. (a) Upper-ocean transport as estimated from AXCP data from Hurricane Norbert (bold vectors) and as simulated by the model (the field of lighter vectors). (b) Mixed-layer currents. The pattern of the mixed-layer current is very similar to that of the transport since mixed-layer transport dominates the upper-ocean transport. The scales at the top and right of these figures are in the units listed in Table 3. A scale for the nondimensional transport, $\tilde{M} = h\tilde{U}$, and mixed-layer current, $\tilde{U}$, is also shown at upper left along with a scale in dimensional units.

This left-to-right asymmetry in transport amplitude is enhanced slightly by the stronger wind stress amplitude that also occurs on the right side of a moving hurricane (section 2b). However, the factor of 4 difference in transport amplitude across the hurricane track is due overwhelmingly to the asymmetric rotation of the wind stress noted above rather than the comparatively small asymmetry of wind stress magnitude.

The very simple dynamics that lead to the left-to-right asymmetry in transport involve only the local wind stress and the current. Thus, a one-dimensional model can, if driven with the appropriate time-varying wind stress, also simulate this asymmetry (Martin 1982; Forristall et al. 1991).

2) A STATISTICAL CHECK OF THE ESTIMATED WIND STRESS

To test the wind stress in a quantitative way we have computed some simple statistics on the observed and simulated transports and on the differences between the two (Table 4). To estimate the bias in the wind stress we have computed the normalized ensemble mean of the observed minus simulated transport magnitude:

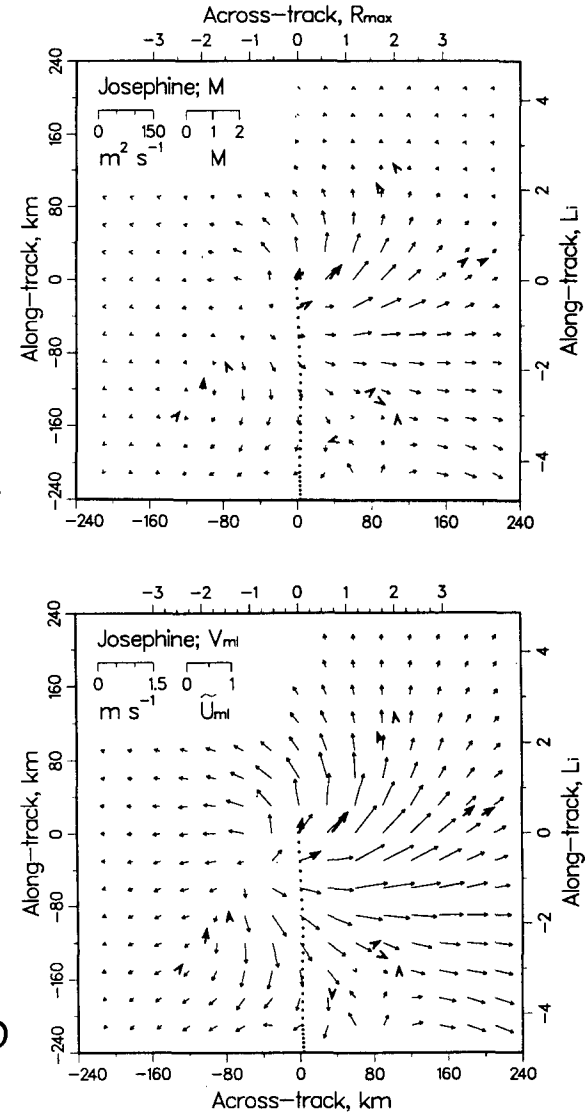

FIG. 5. Same as Fig. 4 but for Hurricane Josephine.

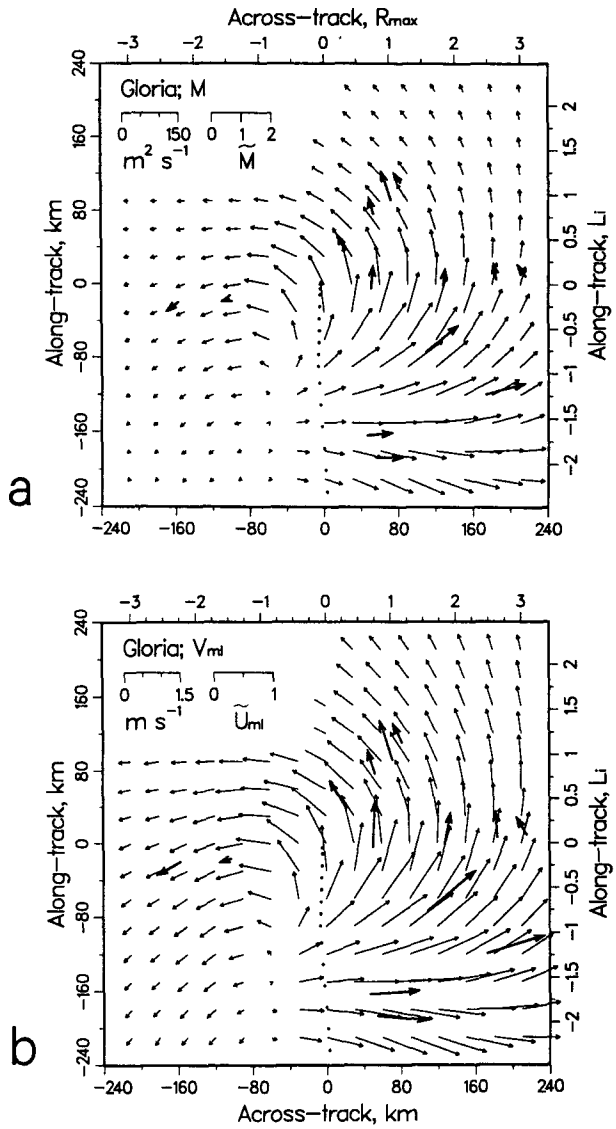

FIG. 6. Same as Fig. 4 but for Hurricane Gloria.

$$\psi M = \frac{\langle M - \hat{M} \rangle}{\mathrm{rms}M},$$

where angled brackets indicate an ensemble average; that is,

$$\langle M^2 \rangle = \frac{1}{N} \sum_{i=1}^{N} (M_i^2),$$

where M_i is the magnitude of the observed transport vector $\mathbf{M}_i$ at AXCP i, and $\hat{M}_i$ is the magnitude of the simulated transport found by interpolating the model solution to the location of AXCP i. The root-mean-square of M is $\mathrm{rms}M = \sqrt{\langle M^2 \rangle}$. To estimate confidence limits on this and other statistics we have computed 90% confidence limits by means of the bootstrap method run over 2000 trials.

On average over all three cases we find that the simulated transport has about the same magnitude as the observed transport (Table 4); that is, $\psi M = -0.05$ $(-0.32, 0.10)$, where the values in parentheses are the lower and upper 90% confidence limits. The sign indicates that the simulated transport is slightly larger than the observed transport. However, given the confidence limits, we would not reject the null hypothesis. Thus, there is no evidence of a substantial bias in the stress amplitude (more than about 20%, given the confidence limits).

Just to be sure that there is some sensitivity in this test we have rerun the simulations using wind stress fields computed from a constant drag coefficient, $C_d = 1.3 \times 10^{-3}$ (and which we would expect to underestimate the stress), in place of the wind speed–dependent form described in section 2b. This gives estimated maximum stresses that are up to 50% smaller than before, and as a direct consequence, the mean difference in transport magnitude becomes $\psi M = 0.28$ (0.02, 0.41). This indicates that the simulated transport is then significantly smaller than the observed transport, as expected, and demonstrates some sensitivity in this test.

A more comprehensive measure of the difference between the observed and simulated transports can be formed from the ensemble average of the mean-square *vector* difference:

$$\Psi\mathbf{M} = \frac{\langle (\mathbf{M} - \hat{\mathbf{M}})^2 \rangle}{\mathrm{rms}M\ \mathrm{rms}\hat{M}} = \Psi M_{\mathrm{mag}} + \Psi M_{\mathrm{dir}},$$

TABLE 4. Statistical comparison of observed–simulated mixed-layer current and upper-ocean transport.

	Full dataset	Weak currents ($V_1 < 0.7$ m s^{-1})	Strong currents ($V_1 \geq 0.7$ m s^{-1})
N	45	24	21
rms$\mathbf{V}_1$, m s^{-1}	0.78	0.39	1.07
rms$\mathbf{M}$, s^2 s^{-1}	45.9	22.0	63.0
ψV	−0.03	−0.27	0.07
	(−0.23, 0.07)	(−0.56, 0.05)	(−0.10, 0.17)
$\Psi\mathbf{V}$	0.18	0.66	0.10
	(0.07, 0.40)	(0.23, 1.20)	(0.03, 0.14)
ΨV_{mag}	0.06	0.17	0.04
	(0.01, 0.10)	(0.01, 0.29)	(0.00, 0.06)
ΨV_{dir}	0.12	0.49	0.06
	(0.03, 0.31)	(0.09, 1.41)	(0.01, 0.09)
ψM	−0.05	−0.19	−0.01
	(−0.32, 0.10)	(−0.50, 0.07)	(−0.32, 0.19)
$\Psi\mathbf{M}$	0.75	0.28	0.20
	(0.14, 0.50)	(0.28, 1.65)	(0.10, 0.32)
ΨM_{mag}	0.12	0.19	0.12
	(0.04, 0.22)	(0.02, 0.42)	(0.03, 0.21)
ΨM_{dir}	0.15	0.56	0.09
	(0.05, 0.33)	(0.11, 1.37)	(0.02, 0.15)

Note: ψV is the ensemble average of the observed minus simulated mixed-layer current amplitude, while $\Psi\mathbf{V}$ is the ensemble averaged vector difference (notation defined in section 4a). The numbers in parentheses are lower and upper 90% confidence limits.

where

$$\Psi M_{\text{mag}} = \frac{\langle \mathbf{M}^2 + \hat{\mathbf{M}}^2 \rangle}{\text{rms}M \, \text{rms}\hat{M}} - 2$$

is the contribution due to differences in magnitude, with $\mathbf{M}^2$ being the dot product of a vector with itself, and

$$\Psi M_{\text{dir}} = 2\left(1 - \frac{\langle \mathbf{M} \cdot \hat{\mathbf{M}} \rangle}{\text{rms}M \, \text{rms}\hat{M}}\right)$$

is the contribution due to differences in direction. Note that ψM could be zero over an ensemble having a large ΨM_{mag}, since the latter depends upon the square of the transport vector difference rather than the magnitudes alone.

Averaging over all three cases ($N = 45$), we find that $\Psi M = 0.28$ (0.14, 0.50) and that $\Psi M_{\text{mag}} = 0.12$ and $\Psi M_{\text{dir}} = 0.15$. Thus, the vector difference is due about equally to differences in direction and magnitude.

Following Willmott et al. (1985), we can define a systematic component of the difference by determining the parameters (an offset $\mathbf{a}$ and stretching, b) of the linear transformation on the simulated transport that minimizes $\Psi\mathbf{M}$. By a search procedure we have found that $\mathbf{a} = (2.9, 4.7)$ m^2 s^{-1} and $b = 0.95$ give the minimum, $\Psi\mathbf{M} = 0.25$. The offset has no obvious physical interpretation; the optimal stretching is to reduce the simulated transports by 5%, which is consistent with the $\Psi\mathbf{M}$ noted above. That is, a better solution would result from reducing the applied wind stress by 5%. However, the optimum $\Psi\mathbf{M}$ is only very slightly smaller than the value obtained straightaway so that most of $\Psi\mathbf{M}$ appears to be random, at least when compared to the optimal linear transformation.

b. *Mixed-layer currents*

As a measure of the mixed-layer current we use the mixed-layer-averaged current estimated from the three-layer fit to AXCP data, $\mathbf{V} = \mathbf{V}_1$. The simulated mixed-layer current, $\hat{\mathbf{V}}$, can be taken as the current at the shallowest grid level, $z = -5$ m (Figs. 4b, 5b, and 6b).

1) Horizontal structure and amplitude

The overall pattern of the mixed-layer current is very much like the pattern of the transport, and the previous discussion of the rightward bias holds equally well here. The mixed-layer current field differs from the transport field in that the current amplitude is inversely proportional to the depth over which the wind stress (or transport) is mixed vertically. The depth of vertical mixing is thus an important aspect of the forced stage response that is taken up in section 5.

The mixed-layer current at any one place in the ocean has the time dependence of a near-inertial motion so that the equivalent wavelength along the track is very roughly the inertial wavelength, $2\pi L_i = U_H \times (2\pi/f) \approx (390, 310, 610)$ km in the cases (Norbert, Josephine, Gloria), where U_H is taken from Table 2. Because the hurricanes changed speed and direction as they neared the survey region this estimate of the alongtrack scale is not accurate away from the center of the survey region. In the same way, the nondimensional alongtrack scale is a rough guide only since it does not account for track curvature.

While the storm-centered coordinate system cannot make the solutions completely similar, it does nevertheless help to reveal the case-to-case differences in the horizontal patterns of current and transport, most of which can be attributed to variations in the hurricane size or track. Notice specifically that the overall width of the region of strong response is considerably bigger in the Gloria case than in the Norbert case and, not surprisingly, appears to be proportional to the size of the hurricanes. The Norbert case also shows a region of strong response in the left rear quadrant, which is not seen in the other cases. This is due to the cyclonically curving track that Norbert took upon entering the survey region (Fig. 2).

The maximum observed mixed-layer current varied by a little more than a factor of 2 over these three cases. In the Norbert case the observed maximum current was 1.1 m s^{-1}, in Josephine it was 0.8 m s^{-1}, and in Gloria it was 1.7 m s^{-1}. The scale estimate of the mixed-layer current (Table 3) is nearly equal to the observed values for Norbert and Gloria but is somewhat larger than the actual value found under Josephine. This is likely due to the fact that Josephine moved slowly enough ($S \leq 1$) that the wind stress on the right side of the track rotated more slowly than did the mixed-layer current, and hence was not coupled as efficiently as the scaling assumes (see also Greatbatch 1984).

2) Statistical comparison of observed and simulated currents—The effects of measurement noise and inhomogeneity

We have also computed the scalar and vector differences for mixed-layer currents (Table 4). The vector difference indicates a fairly high skill for the simulation of mixed-layer currents. Averaged over the full dataset, $\Psi\mathbf{V} = 0.18$ (0.07, 0.40), which shows that the model simulation can account for $100(1 - 0.18)\% = 82\%$ of the variance of the observed mixed-layer current.

A careful visual comparison of the observed and simulated currents reveals that simulation skill is strongly inhomogeneous. The large-scale horizontal structure of the current appears to be simulated well in the regions of the strongest current (e.g., the right side of the track in all three cases). However, in regions where the current is weaker, $V_1 < 0.7$ m s^{-1}, most notably in the left rear quadrant of Josephine, a point-by-point comparison of observed and simulated currents indicates poor model skill, including very large

differences in direction. It appears that model skill is highest in the cases with the largest currents (Norbert and Gloria) and, within any particular case, it is highest in regions that have the largest current (to the right of the track of Josephine, for example).

Statistics computed over subsets of the data confirm this impression. The mean-square vector difference computed over the half of the AXCPs having strong currents ($V_1 \geq 0.7$ m s^{-1}, $N = 21$) is $\Psi\mathbf{V} = 0.10$ (0.03, 0.14), which is somewhat better than the overall average. The mean-square vector difference computed over the half of the AXCPs having weak currents ($V_1 < 0.7$ m s^{-1}, $N = 24$) is $\Psi\mathbf{V} = 0.66$ (0.23, 1.20), which is much higher (much less skillful) than the average overall.

The increase of $\Psi\mathbf{V}$ with decreasing V_1 is notable and suggests that some process unrelated to the hurricane response, for example, measurement errors or prehurricane currents, may be contributing significantly to the vector difference. One way to check for this explicitly is to plot the magnitude of the current difference, $V' = |\mathbf{V} - \hat{\mathbf{V}}|$, against the speed of the observed current, which is done in Fig. 7 for all of the AXCP samples. The solid line is the least-squares fit of a straight line. There is a weak tendency for larger differences to occur at larger speeds, which would be expected if the differences were due to a model error of some sort. However, more than 90% of the variance of V' is associated with the mean value, $\langle V' \rangle \approx 0.25$ m s^{-1} rather than the linear component. This indicates that the difference appears to be nearly independent of the amplitude of the current.

In section 2b we estimate that the net uncertainty of interpreting the AXCP current data as a hurricane response was $V_{\text{noise}} = 0.3$ m s^{-1} rms. If this V_{noise} were the sole contributor to the difference between observed and simulated mixed-layer currents, then we would have $\Psi V = (V_{\text{noise}}/\text{rms}V)^2 = (0.3/1.07)^2 = 0.08$ for the subset of strong currents, $\Psi\mathbf{V} = 0.59$ for the subset of weak currents, and a mean value of about $\langle V' \rangle = 0.23$ m s^{-1}. These are only slightly less than the actual ΨV and $\langle V' \rangle$, indicating that V_{noise} is likely to be a major contributor to the difference between the observed and simulated currents.

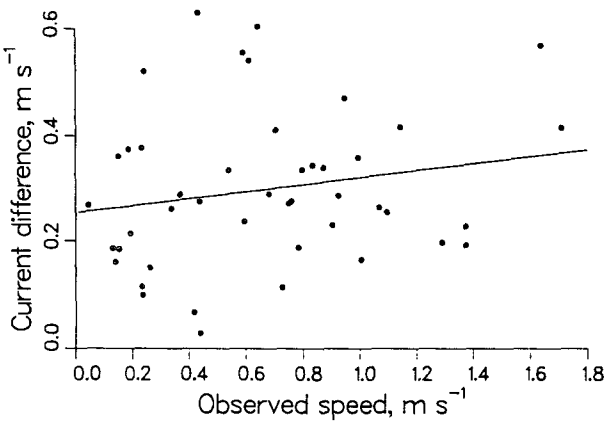

FIG. 7. The speed of the observed minus simulated mixed-layer current (vector difference), plotted as a function of the speed of the observed current. The straight line is a least-squares fit to the data. Note that the speed of the current difference is nearly independent of the speed of the observed current.

5. The upper-ocean thermal response

While we emphasize upper-ocean currents throughout this paper, we consider briefly some aspects of the thermal response in this section. The thermal response is completely intertwined with the current response, and, for example, any model that purports to simulate mixed-layer currents should be held accountable for vertical mixing and the accompanying cooling of the mixed layer.

a. The horizontal pattern of cooling and mixing

Hurricane-forced cooling of the sea surface is a striking phenomenon that is of central importance to the interaction between hurricanes and the ocean (Emanuel 1988). It is also the best-known aspect of the upper ocean's response since it can be observed in satellite imagery (Stramma et al. 1986) and in situ (i.e., Church et al. 1989). For our purpose here, sea surface cooling is useful as a diagnostic of the horizontal structure of vertical mixing.

A graphic and particularly relevant example of sea surface cooling is given by Cornillon et al. (1987), who showed the cool wake of Hurricane Gloria observed in satellite infrared imagery of the western North Atlantic. Gloria caused pronounced cooling of the sea surface over a swath about 400 km wide that extended for almost 2000 km from the subtropics to New England. Cooling was markedly asymmetric, being about four times stronger on the right side of the track than on the left (Fig. 8b). The model simulation of cooling gives a similar result, indicating a reasonable pattern and amplitude of vertical mixing.

As we indicated in section 2a, our AXCP data from the Gloria case give a very muddled view of the same event (Fig. 8a). The reason, we believe, is that one-time survey data do not allow a separation of prehurricane thermal variability from the subsequent cooling caused by the hurricane.

The Norbert AXCP dataset shows a more or less plausible pattern of hurricane-induced cooling (Fig. 9a), including some hints of the rightward asymmetry seen in the satellite data. The maximum amplitude of the observed cooling was only about 2.5°C. The simulated cooling is not inconsistent with this, but the model field suggests that the distribution of the AXCP samples was inadequate to define the horizontal structure of the sea surface cooling and may have missed the largest cooling entirely. Given that much better observations of this phenomenon are extant, we forego further discussion of the horizontal structure.

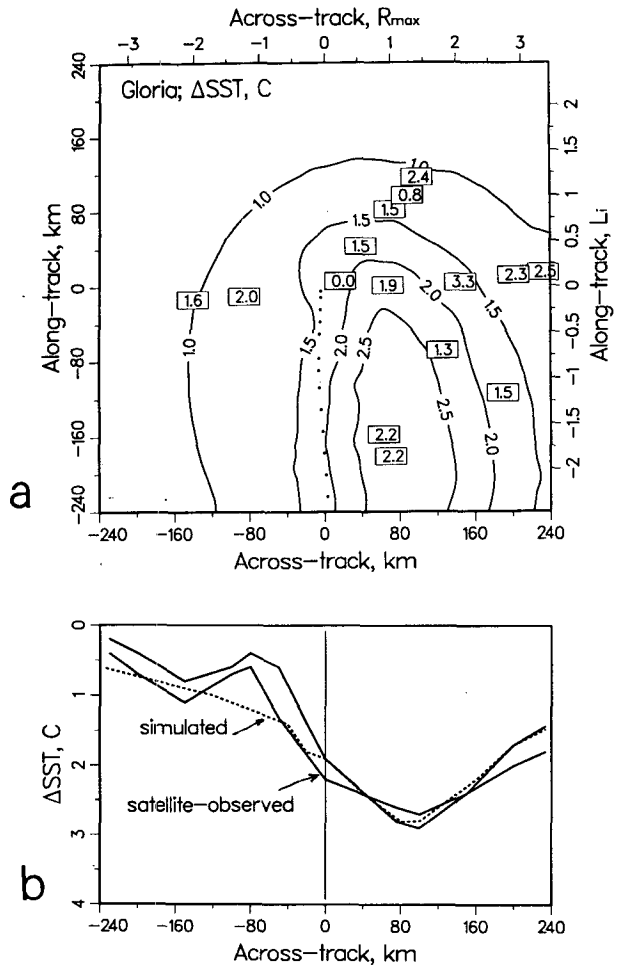

FIG. 8. (a) An estimate of SST cooling made from Gloria AXCP data by subtracting the estimated initial SST, 28°C, from the observed SST at each AXCP (the numbers posted in squares). Also shown is the cooling simulated by the model (the contoured field). Note that the observed cooling is as large under the front half of the storm as it is under the rear half. We infer from this that the apparent cooling is badly contaminated by prehurricane variability. (b) The across-track profile of sea surface cooling in the Sargasso Sea due to Hurricane Gloria as estimated from satellite infrared imagery by Cornillon et al. (1987) (solid lines). The cooling taken from the model simulation shown above is the dashed line.

b. *The vertical profile of cooling*

What we are able to see here in an interesting way is the vertical structure of the cooling. One immediate result is that though there is significant vertical mixing beneath these hurricanes, there is nonetheless only a modest increase in the depth of the surface mixed layer (Fig. 9b). The mixed-layer depth appears to increase from an initial 30 m to perhaps 40–45 m on the right side of the track and close to the center. This is found in both the AXCP data and in the model solution. Some of the increase in mixed-layer depth is offset by upward vertical advection (Greatbatch 1985), which compresses the mixed layer by roughly 15 m on average over the region sampled here (discussed further in section 6a).

Even allowing for advection, the increase in mixed-layer depth seems small and probably gives an underimpression of the intensity of vertical wind mixing. Evidence from field experiments is that much of the vertical mixing driven by storms occurs within the upper thermocline rather than solely within a deepening surface mixed layer. A clear demonstration of this was by Large et al. (1986), who used drifting thermistor string data to examine the change in the upper-ocean temperature profile caused by the passage of strong autumn storms over the eastern North Pacific. They found that midlatitude storms caused cooling within a surface layer that was just slightly thicker than the prestorm mixed-layer depth, h, and significant warming over a sublayer whose thickness was roughly $h/2$. This showed that vertical mixing penetrated well below the depth of the surface mixed layer.

We have estimated the upper-ocean temperature change caused by Norbert by computing the average temperature profile over AXCPs behind the eye of Norbert (AXCPs N3, N13, N14, N15, N23, N24) and then subtracting a presumed prehurricane reference, the temperature from AXCP N2 (Fig. 10a). The composite profile shows very little increase in the mixed-layer depth, which we noted above, and cooling to a depth of at least 150 m. The maximum of cooling occurs at a depth of about 60 m. This profile of cooling is qualitatively different from that found by Large et al. (1986) because of a pronounced effect of upward vertical advection, or "upwelling" for short, that occurs over most of the region sampled behind the eye of Norbert.

The same kind of cooling profile occurs as well in the model solution (Fig. 10b) where we can readily separate the effects of vertical mixing, air–sea heat exchange, and upwelling. To isolate the effects of mixing alone, we can omit all forms of advection and air–sea heat exchange (the latter causes SST cooling of about 0.4°C), and the three-dimensional model becomes an array of one-dimensional upper-ocean models. In that case the simulated cooling profile has the form expected from vertical mixing alone, namely, cooling in an upper layer, nearly coincident with the initial mixed layer, and warming in a lower layer (Fig. 10c). It is noteworthy that the warmed layer, and thus the effect of vertical mixing, penetrates to about 90 m in the absence of upwelling. These model results suggest that the thickness of the warmed layer can be considerably greater than the thickness of the cooled layer, provided that the wind stress is very strong, as it is here. (This analysis yields a spatial average that obscures that mixing penetrates even more than 90 m on the right side of the track and considerably less on the left side of the track.)

With advection included (Fig. 10b), upwelling causes cooling throughout the water column and is suf-

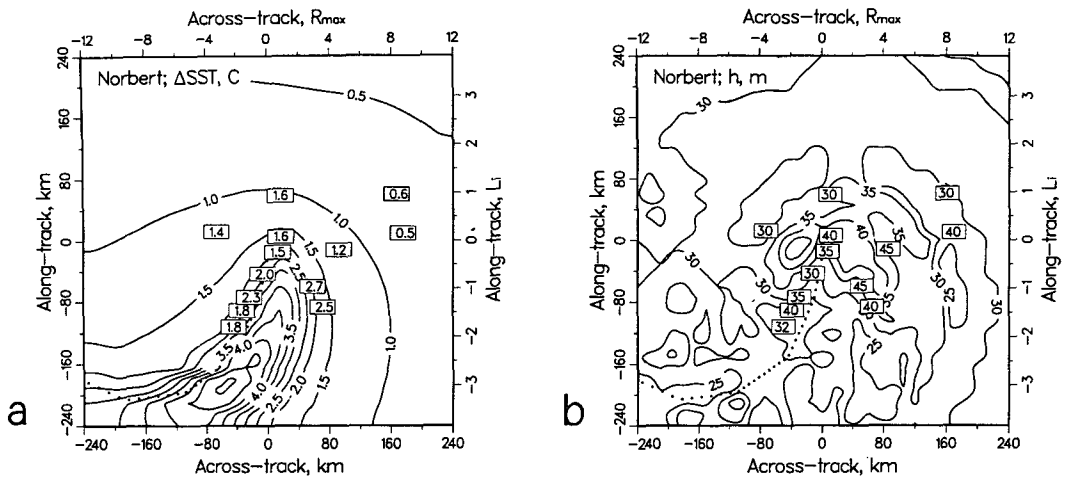

FIG. 9. (a) Observed cooling of the mixed layer from the Norbert case as estimated from AXCP temperature data (the numbers posted in squares and estimating the initial SST as 29°C), and the mixed-layer cooling simulated by the numerical model (the contoured field). (b) The depth of the mixed layer as estimated from AXCP data (posted values) and as simulated by the numerical model (contoured field).

ficient to overwhelm the warming in the transition layer caused by vertical mixing. Indeed, the greatest amplitude of cooling occurs just below the mixed layer where the vertical gradient of temperature is largest. From this we can see that while vertical mixing dominates the heat budget of the mixed layer, upwelling dominates the heat budget for a deeper water column. [In regions far from the eye, where the wind stress curl was negative, we would expect to find a compensating downwelling that would cause warming within the thermocline (Price 1981).]

c. *Estimates of the Richardson numbers*

The mixing parameterization used here becomes active when either the bulk Richardson number for the mixed layer (R_b) reaches its "critical" value of 0.65 or when the gradient Richardson number (R_g) reaches its critical value 1/4. [Trowbridge (1992) shows that these may be equivalent under some circumstances.] If a mixing parameterization of this sort were indeed appropriate, then we should observe that both R_b and R_g are near their critical values in regions of strong mixing, for example, near the eye and especially to the right of the track. They might take on larger values in outlying regions.

It is surprisingly difficult to evaluate the Richardson numbers from AXCP data because of uncertainty in estimating the length scales in the numerators. This is especially true for R_b since the mixed layer merges smoothly into the transition layer, which merges smoothly into the thermocline. (This is also true in the model profiles of Figs. 10, 12, 13, and 14.) In the regions of strongest mixing we would expect that the full thickness of the transition layer would be mixing actively and that the appropriate length scale for R_b would then be $h + d/2$, where d is the thickness of the transition layer estimated from the three-layer profile fit to the AXCP current data as $d = -(Z_2 - Z_1)$ (data are in Table 2A). The length scale for R_g is just d, and so the ratio $R_g/R_b = d/(h + d/2)$. We estimate the density difference to be $\delta\rho = \alpha\delta T$, where δT is the temperature change across the transition layer (listed in Table 1A), α is the thermal expansion coefficient (-0.32 kg m^{-3} C^{-1}) (and where salinity has to be neglected since it was not measured by AXCPs), and the current difference is estimated to be $\delta\mathbf{V} = \mathbf{V}_1 - \mathbf{V}_3$, where $\mathbf{V}_3$ is the thermocline current. In profiles where the mixed-layer current is large (greater than about 0.7 m s^{-1}), there is generally a well-defined transition layer with a clear δT. In such profiles R_b is then fairly well defined from the field data. However, where the mixed-layer current is small (left of the track and ahead of the eye), there is only a thin and sometimes indistinct transition layer, and this analysis is liable to overestimate Richardson numbers.

In the regions farthest from the eye and that have weak mixed-layer currents, the Richardson numbers are likely to be imprecise owing to uncertainty in defining the transition layer; nevertheless, the AXCPs and Richardson numbers are (AXCP$_i$; R_b, R_g), (N2; 4.8, 2.9), (N4; 5.6, 2.0), and (N26; 5.9, 6.5). These are all quite a lot larger than the critical values. In the region close to the eye but to the left of the track the values are rather scattered: (N18; 3.2, 1.3), (N20; 0.9, 0.5), (N21; 2.6, 1.5), and (N3; 0.6, 0.3). The smallest R_b and R_g are found in a region near the eye and to the right of the track, which is also the region where vertical mixing is likely to be strongest (cf. Fig. 9a). The values are (N31; 0.8, 0.6), (N15; 0.8, 0.4), (N16; 0.8, 0.5), (N6; 0.9, 0.2), (N13; 0.7, 0.4), and (N14; 0.5, 0.3). Thus, the typical values in the region of strong

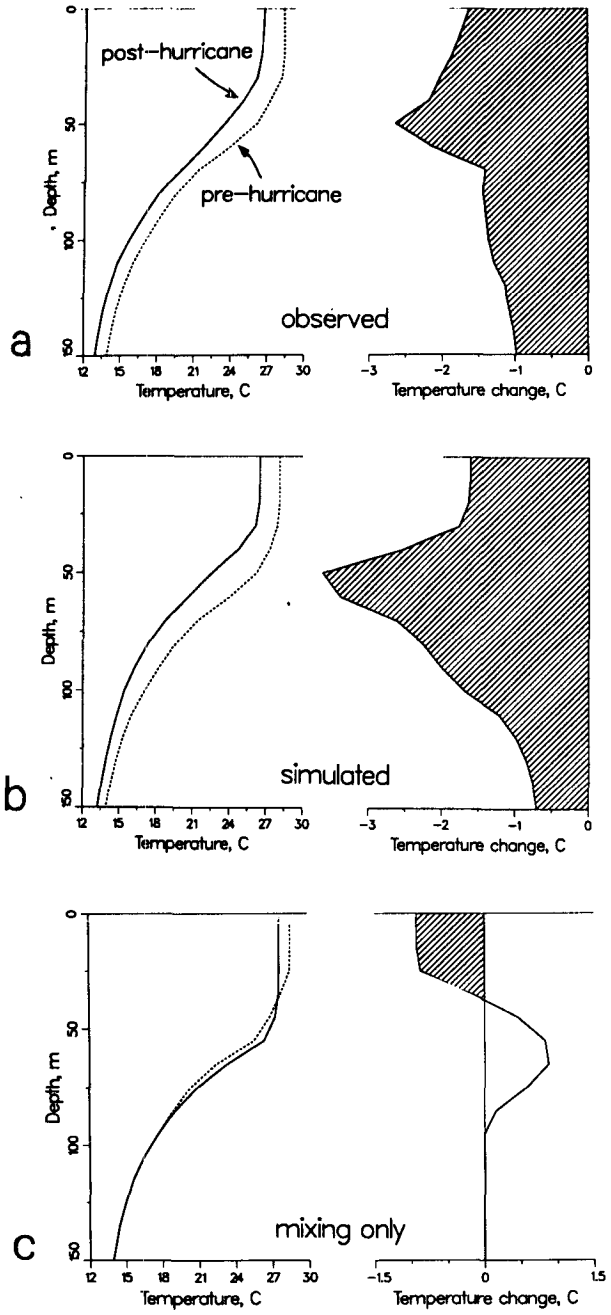

FIG. 10. (a) Temperature profiles from AXCP data taken under the leading edge of Hurricane Norbert (the dotted profile, AXCP N2, which probably has about 0.5°C of mixed-layer cooling due to the approaching hurricane), and the average temperature profile from all AXCPs behind the hurricane eye (solid line). The single curve on the right shows the resulting change in temperature (note the scale change for temperature). (b) Pre- and posthurricane temperature profiles taken from the model solution at the same locations as the AXCP data used in the panel above. (c) Pre- and posthurricane temperature profiles taken from the model solution but with vertical mixing only (no air–sea heat exchange and no advection). Note that the region of warming extends to a depth of about 90 m, or comparable to the mixed-layer thickness.

mixing are about $R_b \approx 0.7$ and $R_g \approx 0.4$, which are not inconsistent with the mixing parameterization. [Shay et al. (1989) mentioned a similar result for the bulk Richardson number.]

6. The beginning of the relaxation stage response in the thermocline

An important and at first surprising result of the S87 field study was the observation of substantial thermocline-depth currents under the rear half of Hurricane Norbert. (Figure 11a shows a plan view; Figs. 12, 13, and 14 show individual profiles.) The presence of these large thermocline currents suggests that the nonlocal dynamics of the relaxation stage response may have been important even during the forced stage response to Norbert; as we will show, this can be understood as a consequence of the large Burger number in that case. We should note that the sampling by AXCPs was not designed to resolve the thermocline response, and consequently the available data give a limited view. Only about six AXCP samples show a strong thermocline response and by themselves would not serve to define the horizontal structure. (The vertical structure is quite simple and well defined, as we will discuss). Fortunately, the model gives a plausible simulation of the thermocline currents and can help to show how these thermocline currents are generated by the hurricane. [See also Shay et al. (1989), who model the thermocline response by a summation of normal modes.] Like the transport, the thermocline response is independent of model-specific parameterizations and would be found in a very similar form in any other three-dimensional primitive equation ocean model driven by the same hurricane.

a. Upwelling

The thermocline response begins when there is a pressure gradient produced by some sort of density anomaly, which may in turn be due to mixing or advection. Upwelling is the most important mechanism of density change in the hurricane response and is driven by the wind stress curl of the hurricane by way of a divergent upper-ocean transport. With some guidance from the simulated fields one can see that the upper-ocean transport (Fig. 4a) is strongly divergent in a region just behind the hurricane eye; the transport to the right of the track flows to the right with a large amplitude, while the transport to the left of the track flows away from the track but is much weaker. This divergence must act to cause a depression in the sea surface and an upwelling of the thermocline (it also compresses the mixed layer as noted in section 5b). We cannot see the sea surface height anomaly in these data but we can detect the upwelling as a cool anomaly within the upper thermocline; the amplitude of upwelling is estimated from the AXCP data as the dis-

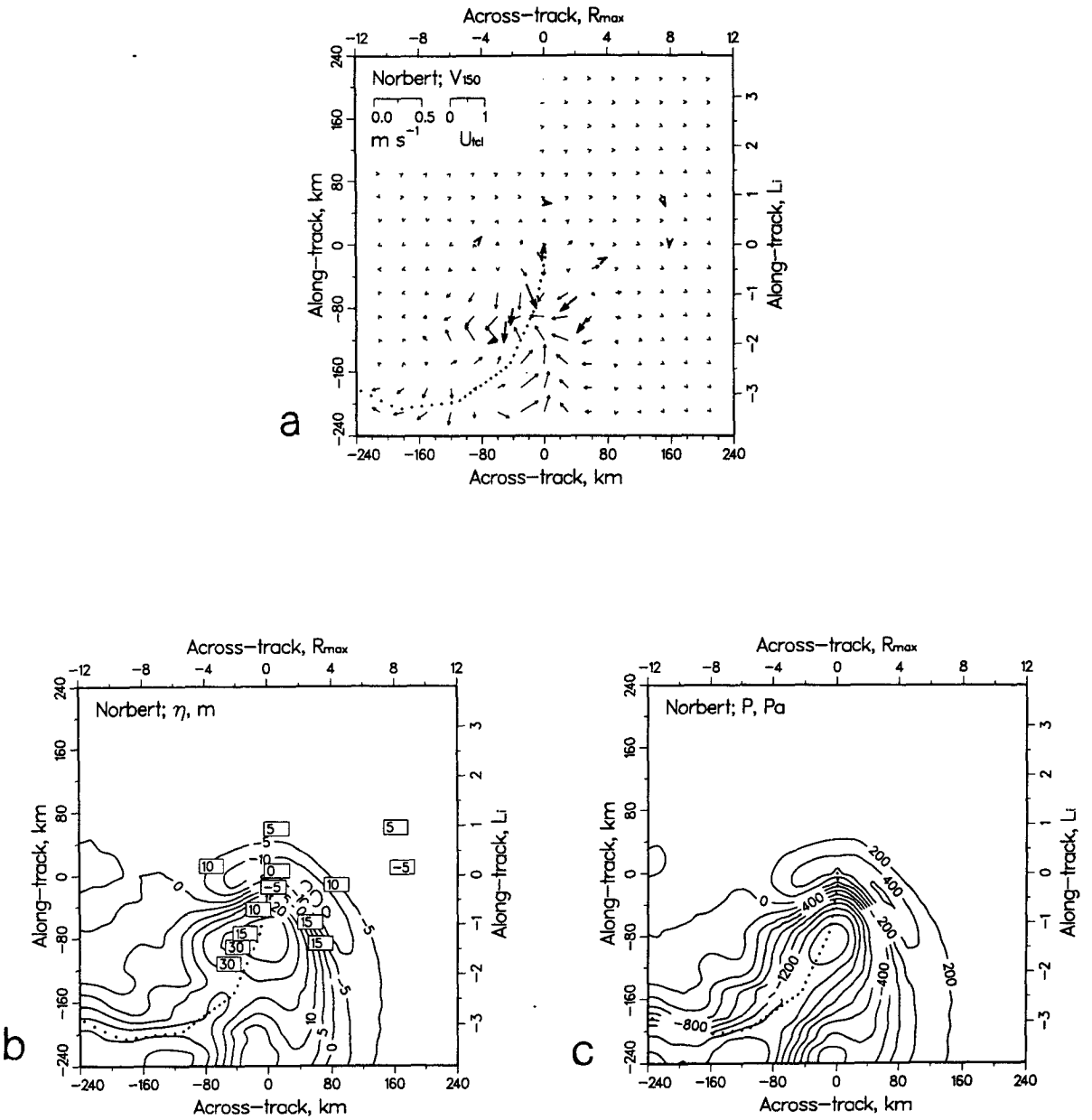

FIG. 11. (a) Thermocline-depth currents (150-m depth) from the Norbert case. Observed currents are the bold vectors; the simulated currents are the field of lighter vectors. (b) Upwelling as estimated from the displacement of the 14°C isotherm (posted values) and as simulated (contoured field). (c) Pressure anomaly from the numerical simulation (no field data shown here). Note that the upwelling region located about 100 km behind the hurricane eye has an associated low pressure anomaly of about 1400 Pa.

placement of the 14°C isotherm from its initial level. Because Norbert was both intense and comparatively small, the upwelling had a fairly large amplitude, the simulations suggesting that the maximum $\eta \approx 40$ m or comparable to the mixed-layer thickness. The largest upwelling seen in the data was less, about 25 m, but the simulations suggest that the largest upwelling and thermocline currents may have occurred 100 km or more behind the hurricane eye in an area that was not sampled by AXCPs.

The mixed-layer transport oscillates with a near-inertial period, and hence so does the divergence and the associated upwelling and downwelling, which has been termed "inertial pumping" (Price 1983; examples from field data that show this time dependence are in Price 1981; Brooks 1983; Shay and Elsberry 1987). The area shown in Fig. 11b covers a little less than one inertial wavelength along the track. Looking from front to rear along the track, we can see only about the first cycle of the inertial pumping (and this is much clearer in

the simulated upwelling field than it is from the field data alone). In the Norbert case the Mach number was fairly small, $C \approx 1.5$, so that the upwelling also includes a substantial steady component, and some upwelling occurs directly under the storm (Geisler 1970).

b. *Horizontal structure and amplitude of the thermocline currents*

The dynamic effect of the upwelling is to produce a hydrostatic pressure anomaly within the mixed layer and the main thermocline. The region of upwelling (and depressed sea surface height) about 100 km behind the hurricane eye is a region with a low pressure anomaly of about 1500 Pa (Fig. 11b) from the model solution; the scale estimate from Table 3 is

$$\tilde{P} = \rho_0 g' \tilde{\eta}_1 \approx \frac{g'\tau}{fU_H} = 1100 \text{ Pa}.$$

The thermocline-depth currents have a fairly complex and small-scale horizontal structure since they are forced by the horizontal gradient of this pressure anomaly, which has both an alongtrack component $\sim f/U_H$ and an across-track component $\sim 1/R_{\max}$. For the moment we will ignore the alongtrack component, and thus a rough estimate of the pressure gradient acceleration in the upper thermocline is just $A \approx P/(\rho_0 R_{\max})$. The amplitude of the upper-thermocline current produced during the hurricane passage is then estimated to be approximately

$$\tilde{U}_{tcl} \approx \frac{2AR_{\max}}{U_H} \approx \frac{g'\tau}{\rho_0 f U_H^2} \approx \tilde{U}_{\text{ml}} B \frac{\pi}{2S} \approx 0.3 \text{ m s}^{-1}. \quad (13)$$

This is roughly consistent with the amplitude obtained from the numerical model and with the observed thermocline currents. (If we had kept the alongtrack component rather than the across-track component, the S dependence would disappear.) With some effort one can infer that the dominant pattern of the thermocline currents found behind the eye of Norbert (Fig. 11a) is an acceleration toward the low pressure region found about 100 km behind the eye together with an inertial rotation.

c. *The vertical structure of the thermocline current*

The vertical structure of the response is well defined by the Norbert dataset and is easy to understand as a consequence of the pressure forcing described above. It is useful to first mention that under the forward half of the hurricane there was very little upwelling and minimal pressure coupling. Hence, the currents under the forward half of the hurricane are still trapped within the mixed layer and transition layer (Fig. 12).

Under the rear half of the hurricane there is appreciable upwelling and pressure coupling, but the vertical structure of the response is still quite simple during at least the very early part of the relaxation stage that we can see here. At this time the upwelling has a nearly uniform phase and amplitude through the thermocline (Price 1981; Brooks 1983). Using this, and given that the density perturbation is approximately $\eta \partial\rho/\partial z$, then from (8) we would expect that the pressure anomaly should decrease from the surface downward as

$$\frac{P(z)}{P(0)} = \frac{\rho(z) - \rho(z_a)}{\rho(0) - \rho(z_a)},$$

where $\rho(z_a)$ is the density at the top of the abyssal ocean (or the base of the thermocline). Over the upper 200 m shown in Figs. 13 and 14 the temperature decreases by about half of its total change across the thermocline, and hence, we would expect that the pressure anomaly and the thermocline current amplitude should decrease similarly. The observed profiles exhibit a rather gradual monotonic decay with depth, which is not inconsistent with this. Thermocline currents have a nearly uniform direction with depth, which can also be attributed to the nearly depth-independent upwelling. As the relaxation stage response continues to develop during the next several days to weeks, this structure will probably become more intricate (Gill 1984). Brink (1989) has observed the thermocline-depth currents in the Gloria case in moored array data and found that the direction change across the thermocline grew to more than half a cycle within a week after the hurricane passage.

d. *Energy dispersion and Burger number dependence*

Equation (13) shows that the thermocline current scales with the Burger number, B, which is thus a direct measure of the amplitude of pressure coupling between the mixed layer and the thermocline. The Burger number is comparatively large in the Norbert case mainly because Norbert has a small $R_{\max}$, only about 20 km. We would expect weaker coupling in the case of larger hurricanes (Josephine or Gloria), or midlatitude storms, which are generally larger and also have greater f. In the latter case, beta effects may be more important than the coupling produced by the storm scale itself (D'Asaro 1989).

The energy of the thermocline currents must come from the kinetic energy of the wind-driven mixed-layer currents. Thus, the pressure field that drives the thermocline currents must, on average over the entire region, work against the mixed-layer currents as part of a two-way interaction that disperses energy from the region of the forced stage and yet conserves total energy. It is interesting to note that the phase difference between the mixed-layer current and the upper-thermocline current can be 180 deg, as in AXCP N13 (Fig. 13a), or nearly zero as in N21 (Fig. 14b). In the latter case the pressure coupling between the mixed layer and the thermocline would serve to *increase* the mixed-layer current.

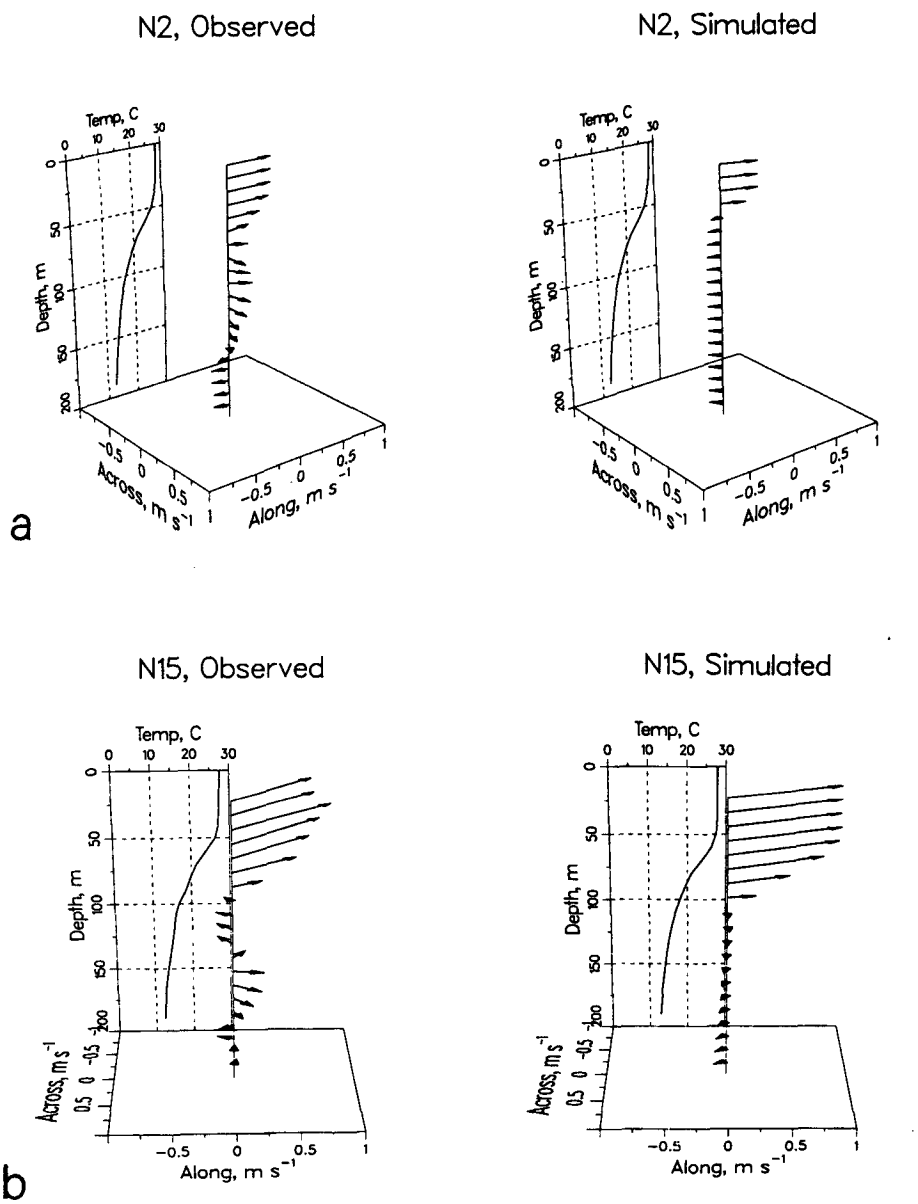

FIG. 12. Current and temperature profiles from Norbert AXCP N2 (a) and N15 (b) and from the simulation at the same locations (right side). In this and in the next two figures, the AXCP data are shown in a nearly raw form, the only data processing being a boxcar smoothing over an interval of 10 m. These two profiles were taken ahead of (N2) or directly under the hurricane eye (N15), and show very little thermocline-depth current. (The roughly 100-m vertical wavelength oscillation found below the mixed layer is thought to be from ambient internal waves.) In this region the hurricane response is largely confined to the mixed layer and transition layer.

Energy dispersion causes the mixed-layer current to decay with an *e*-folding time of typically 5–10 days (Price 1983). From the scale analysis above we would expect that this time scale depends directly upon the Burger number, and when the Burger number is as large as it is in the Norbert case, then the relaxation stage dynamics might be important even during the brief time of the storm passage. We can test this with numerical experiments; if the pressure coupling is arbitrarily suppressed in the Norbert simulation, then the maximum, simulated mixed-layer current increases by about 35% over its nominal value. From this we would conclude that the nonlocal dynamics of the relaxation stage response should be included in simulations of the forced stage response to hurricanes having an appreciable Burger number.

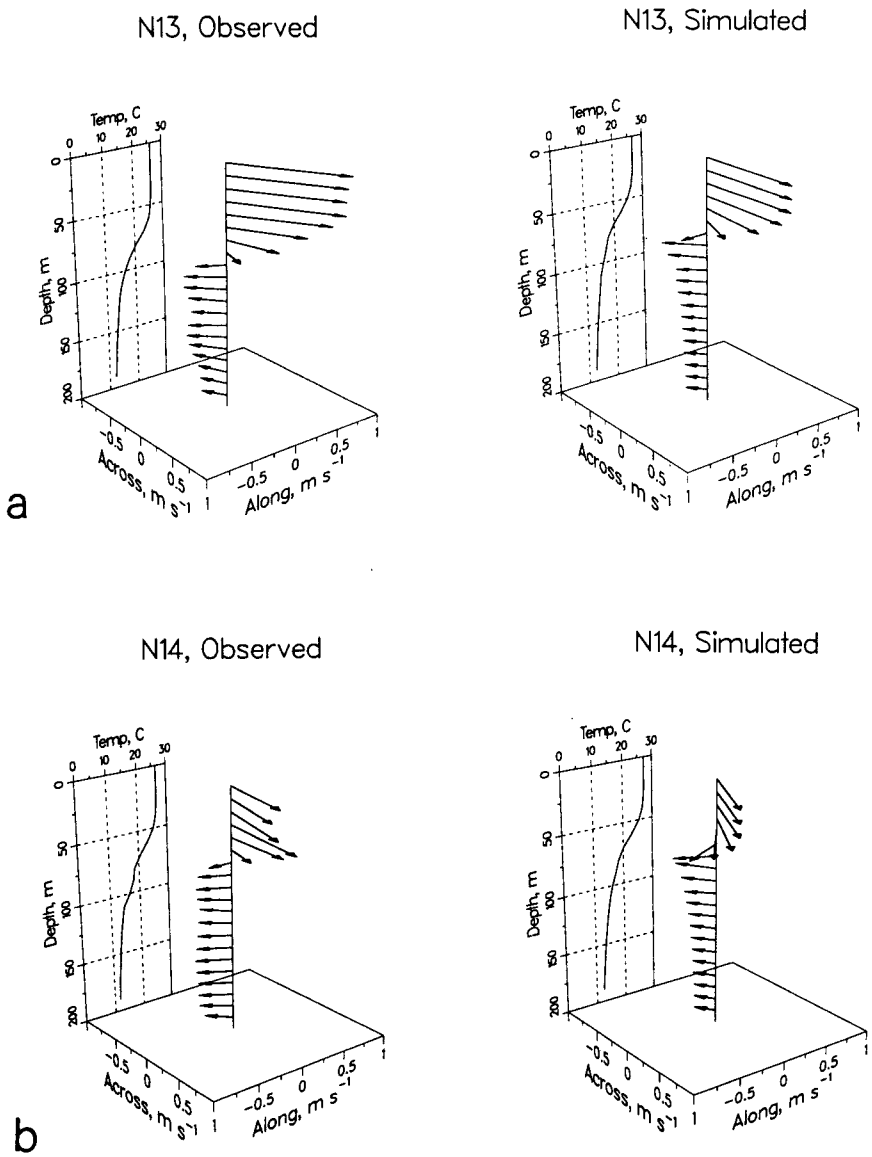

FIG. 13. Current and temperature profiles from Norbert AXCP N13 (a) and N14 (b) and from the simulation at the same locations (right side). At this location, which was behind and to the right of the eye, there is an appreciable thermocline-depth current (depths below 70 m) that flows toward the low pressure anomaly centered about 100 km behind the eye (cf. Fig. 11a). Note that these data (and the data in Figs. 12 and 14) may be used to make rough estimates of the Richardson numbers for the mixed layer and transition layer (the thermal expansion coefficient is about -0.32 kg m^3 C^{-1}).

7. Conclusions and remarks

This and S87 taken together demonstrate the great potential that aircraft-deployed expendable instruments can bring to studies of air–sea interaction. Aircraft can provide oceanographic sampling in definite relationship to synoptic weather and can acquire data in extremely severe weather conditions. Well-equipped aircraft, such as the NOAA P3, can also provide a very high quality measurement of winds, which is crucially important for modeling purposes. However, our problems with the interpretation of the Sargasso Sea datasets should be a caution to future investigators that one-time survey data of the kind readily acquired by aircraft will not always be sufficient to sort out the storm-driven response from preexisting currents and especially thermal variability. To improve significantly upon these field studies it may be necessary to acquire initial survey data

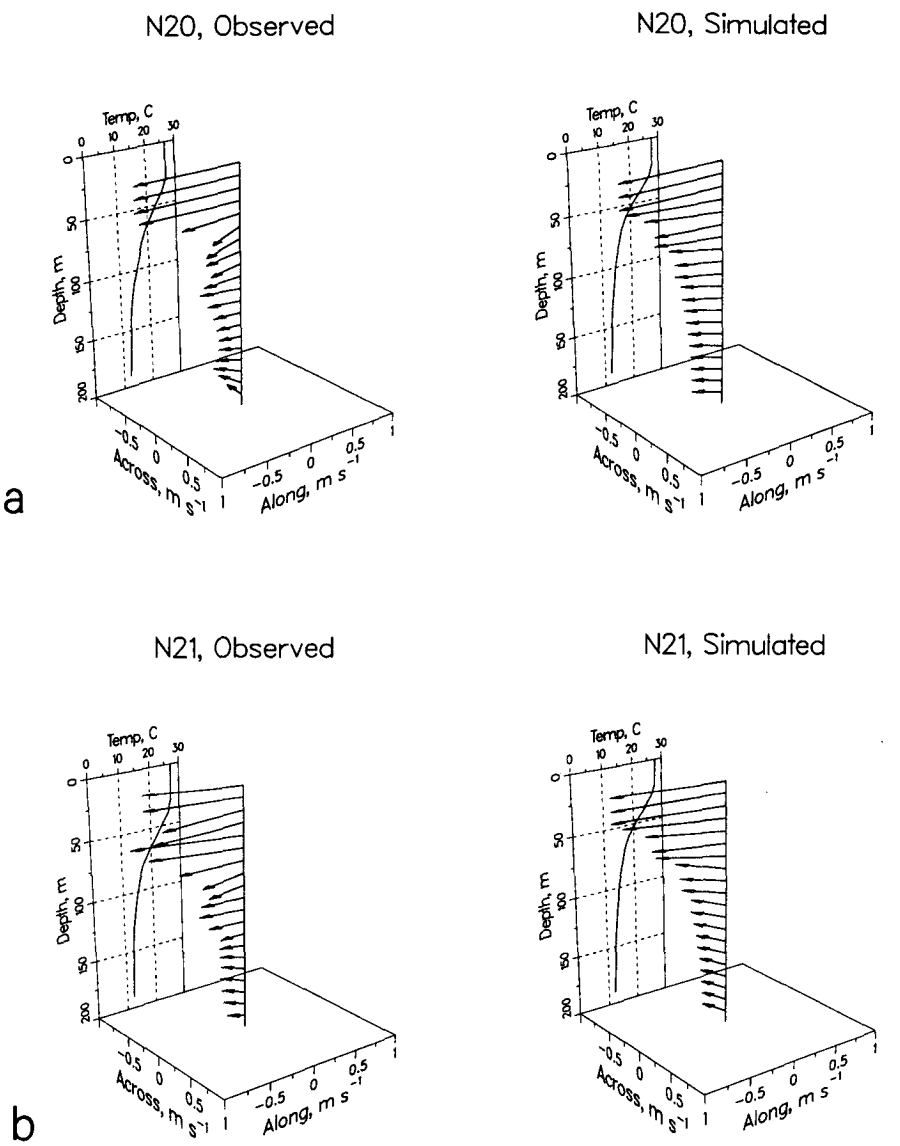

FIG. 14. Current and temperature profiles from Norbert AXCP N20 (a) and N21 (b) and from the simulation at the same locations (right side). At this location, which was behind and to the left of the eye, there was an appreciable thermocline-depth current flowing toward and slightly to the right of the low pressure anomaly centered about 100 km behind the eye (cf. Fig. 11c).

and, just as important and perhaps more effective, avoid regions of high ambient variability.

The practical goal of this study, which was to simulate storm-driven currents for design purposes, was partially realized. The largest currents are simulated rather well in the sense that the model simulation can account for about 90% of the variance in currents greater than 0.7 m s^{-1} (which is about half of the entire dataset). It remains that the overall accuracy demonstrated for these model simulations (rms differences between observed and simulated currents of 0.35 m s^{-1}) is marginally adequate for some design purposes. There is evidence that much of this difference may arise from the noise component of the observed current (due to measurement and analysis error and to pre-hurricane currents), which future field studies should seek to minimize, perhaps as we have indicated here (and see also remarks in S87).

The reasonably good comparison between the observed and simulated strong currents encourages us to think that the simulated current field can be used as a guide for evaluating the AXCP sampling. It appears that the AXCP sampling succeeds in defining the gross horizontal structure of the mixed-layer current, and

especially the large amplitude currents found on the right side of the track of Norbert and Gloria (it was less satisfactory for Josephine). The sampling was not adequate to fully define the horizontal structure of the thermocline response and could be improved in future studies by taking samples on a line 100 or 200 km behind the storm and across the track.

The scientific goals of this study were somewhat more open ended but also partially realized here by showing how the horizontal structure of the forced stage response is imposed by the atmospheric forcing, and by helping to show what processes control the response amplitude. Five specific points are as follows.

1) We found that, for the purpose of simulating ocean currents, the hurricane wind stress fields can be estimated from aircraft-measured winds to within an accuracy of about 20% by means of straightforward, conventional methods. Subhurricane-scale errors may well be present in the stress fields but are not large compared to the "noise" component of the measured current.

2) The horizontal structure of the forced stage mixed-layer response can be understood qualitatively as the local response of the ocean to a time-varying wind stress. If a storm has a nondimensional speed S of O(1), as most hurricanes do, then the upper-ocean response is dominated by near-inertial currents. At locations where the stress turns in the sense of an inertial current (right side of the track in Northern Hemisphere cases), the response will be maximum. The alongtrack scale is roughly the product of the storm translation speed and the local inertial period. The across-track scale of the response is set directly by the horizontal scale of the hurricane itself.

3) Vertical mixing is intense during the forced stage response and can penetrate to depths well below the surface mixed layer. Nevertheless, the depth of the surface mixed layer may show only a modest increase. The profile of ocean cooling behind a hurricane can be radically different from that found behind midlatitude storms because of a pronounced effect of upwelling.

4) The bulk Richardson number assumes values a little less than 1 in the regions of the largest mixed-layer currents near the eye and to the right of the track. In the same regions the gradient Richardson number is near its critical value (1/4) within a thick transition layer below the mixed layer.

5) In the Norbert case, which had an appreciable Burger number, $B \approx 1/2$, we can see the beginning of the relaxation stage response. There was upwelling of roughly 25 m and thermocline-depth currents of up to 0.3 m s^{-1} beneath the rear half of the hurricane. These thermocline-depth currents have very little phase change with depth and a monotonically decreasing amplitude. Their horizontal structure can be understood as an acceleration toward a low pressure region behind the storm.

Acknowledgments. The field programs that made this study possible were supported by a Joint Industry Program entitled Ocean Response to a Hurricane; corporate members were Amoco Production Co., Arco Oil and Gas Co., Chevron USA Inc., Conoco Inc., Exxon Production Research, Gulf Oil Exploration and Production Co., Marathon Oil Co., Mobil Research and Development Co., Shell Development Co., and Sohio Petroleum Co. Guidance and encouragement were provided by a technical committee chaired by James Haustein; members were Gene Berek, Thomas Mitchell, James Allender, Robert Gordon, David Peters, Michael Feifarek, Irving Brooks, and Sherman Chiu. The authors are grateful to all of those who participated in the technical developments and flight operations that made the measurements possible. Field operations and program management were conducted by James Feeney of Horizon Marine, assisted by William Kucharski and Jennifer Briggs. Development of AXCP hardware was carried out by Robert Drever of the University of Washington Applied Physics Laboratory. Flight operations were supervised by Peter Black of the NOAA Hurricane Research Division and Jan Zysko of the NOAA Office of Aircraft Operations. J. F. Price and T. B. Sanford were supported by the Office of Naval Research during the period of manuscript preparation.

APPENDIX

AXCP Data Analysis and Listings

The currents inferred directly from AXCP measurements are relative currents because of an unknown

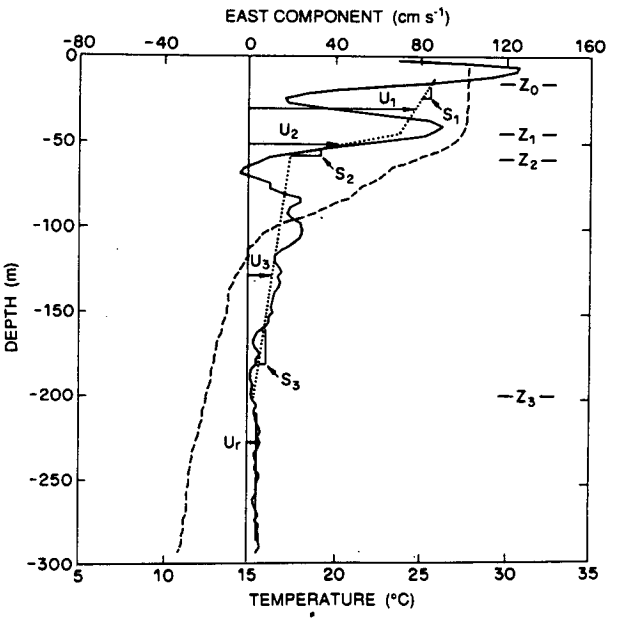

FIG. A1. Three-layer model fit to an AXCP current and temperature profile (from Sanford et al. 1987).

TABLE A1. AXCP station data and layer depths. In column one D is the AXCP number; N denotes Norbert; J, Josephine; G, Gloria. F/S indicates fast- or slow-fall probe. X and Y are the across-track and alongtrack coordinates of the storm-centered system. TML is temperature of the surface mixed layer, and δT is the temperature change across the transition layer. η is the apparent upwelling within the thermocline. Z_i is the depth of layer i. a: AXCP G19 did not go deep enough to measure layer 3.

D	F/S	lat (°N)	long (°E)	Date	Time (UTC)	X (km)	Y (km)	TML (°C)	δT (°C)	η (m)	Z_1 (m)	Z_2 (m)	Z_3 (m)
N2	F	20.56	−108.20	23Sep84	2244	150.2	54.5	28.4	2.5	−5.	−30.	−55.	−200.
N3	F	18.11	−108.76	24Sep84	17	−61.1	−117.9	27.2	5.0	20.	−32.	−50.	−200.
N4	F	20.25	−107.86	23Sep84	2253	158.4	3.8	28.5	3.0	0.	−40.	−60.	−200.
N6	F	19.60	−108.33	23Sep84	2311	74.9	−17.9	27.8	3.0	0.	−45.	−60.	−200.
N13	F	19.07	−108.31	23Sep84	2335	41.2	−65.9	26.3	5.0	0.	−45.	−80.	−200.
N14	F	18.96	−108.07	23Sep84	2339	54.3	−92.5	26.5	3.0	15.	−40.	−65.	−200.
N15	S	19.41	−109.08	24Sep84	112	0.0	0.0	27.4	5.0	0.	−40.	−65.	−200.
N16	S	19.20	−108.95	23Sep84	2359	−4.2	−13.8	27.5	5.0	−5.	−35.	−60.	−200.
N18	F	18.83	−108.88	24Sep84	5	−23.0	−49.5	27.0	5.0	5.	−30.	−45.	−100.
N20	F	18.51	−108.83	24Sep84	11	−40.3	−79.8	26.7	5.0	5.	−35.	−60.	−200.
N21	F	18.33	−108.80	24Sep84	13	−49.8	−96.7	27.2	8.0	15.	−40.	−75.	−150.
N22	S	18.88	−108.93	24Sep84	30	−23.6	−46.2	26.9	4.0	20.	−30.	−45.	−150.
N23	S	18.90	−108.83	24Sep84	31	−13.7	−51.9	26.9	4.5	10.	−30.	−45.	−150.
N24	S	18.91	−108.93	24Sep84	31	−21.5	−43.9	26.9	5.0	10.	−35.	−50.	−150.
N26	F	18.93	−109.68	24Sep84	101	−83.6	6.2	27.6	3.0	5.	−30.	−50.	−200.
N31	F	19.81	−109.40	24Sep84	123	−0.1	53.1	27.4	5.5	5.	−30.	−50.	−200.
J2	F	28.61	−73.77	11Oct84	1306	−130.5	−147.7	25.1	2.0	40.	−65.	−75.	−200.
J3	F	28.83	−73.48	11Oct84	1300	−103.1	−119.8	26.0	3.0	25.	−80.	−90.	−200.
J4	F	29.03	−73.20	11Oct84	1255	−76.3	−94.2	24.8	2.0	65.	−45.	−55.	−200.
J7	F	29.37	−72.28	11Oct84	936	0.0	0.0	25.7	2.0	−5.	−75.	−90.	−200.
J8	S	29.07	−72.22	11Oct84	931	11.1	−26.3	26.0	2.0	0.	−45.	−60.	−200.
J13	F	29.28	−70.52	11Oct84	1004	196.7	19.2	24.7	2.5	75.	−40.	−55.	−200.
J14	S	29.30	−70.70	11Oct84	1001	176.4	18.3	24.5	3.0	75.	−50.	−65.	−200.
J17	S	29.33	−71.97	11Oct84	943	35.3	0.6	25.8	2.0	−15.	−70.	−90.	−200.
J20	S	30.40	−71.38	11Oct84	1041	87.2	101.2	24.4	2.5	55.	−55.	−70.	−200.
J21	F	30.66	−71.20	11Oct84	1054	103.8	126.6	24.7	3.0	65.	−43.	−53.	−200.
J25	F	27.93	−71.76	11Oct84	912	78.9	−122.0	25.9	1.5	0.	−60.	−67.	−200.
J26	F	27.75	−71.65	11Oct84	909	93.7	−136.4	26.2	1.5	−5.	−65.	−75.	−200.
J27	F	27.57	−71.55	11Oct84	903	107.1	−150.3	26.0	2.5	5.	−70.	−80.	−200.
J29	F	27.41	−72.23	11Oct84	854	34.5	−176.7	26.0	2.0	30.	−30.	−50.	−200.
G5	S	28.31	−74.09	26Sep85	950	46.0	−163.4	25.8	4.5	15.	−33.	−76.	−200.
G7	S	28.15	−73.90	26Sep85	946	54.1	−186.8	25.8	4.0	0.	−40.	−75.	−200.
G11	S	29.86	−74.22	26Sep85	833	127.9	−1.4	24.7	2.0	55.	−51.	−58.	−200.
G12	S	29.40	−74.78	26Sep85	842	50.6	−4.7	26.1	5.0	45.	−33.	−69.	−200.
G13	S	28.46	−75.87	26Sep85	903	−102.5	−16.2	26.0	4.5	45.	−44.	−78.	−200.
G15	S	28.13	−76.26	26Sep85	910	−156.9	−19.6	26.4	2.5	−25.	−36.	−65.	−200.
G16	S	30.23	−73.83	26Sep85	825	184.6	5.6	25.7	2.0	−45.	−50.	−69.	−200.
G17	F	30.43	−73.61	26Sep85	821	216.1	8.6	25.5	1.5	−35.	−55.	−73.	−200.
G18	F	29.95	−74.89	26Sep85	604	82.1	110.2	25.6	1.5	−15.	−40.	−55.	−200.
G19	F	29.79	−74.89	26Sep85	620	71.9	91.1	27.2	3.0	a	−75.	−113.	a
G21	S	29.47	−74.91	26Sep85	558	53.2	76.1	26.5	3.5	−80.	−53.	−80.	−200.
G24	S	28.93	−74.92	26Sep85	550	21.9	37.5	26.5	4.5	30.	−45.	−65.	−200.
G25	F	28.91	−73.16	26Sep85	729	172.8	−119.4	26.5	3.5	−50.	−58.	−84.	−200.
G27	S	28.87	−73.85	26Sep85	720	109.0	−73.8	26.7	4.0	−40.	−55.	−95.	−200.
G31	F	28.68	−77.00	26Sep85	637	−182.4	134.5	27.7	3.0	−80.	−57.	−66.	−200.

offset or reference current, U_r, which is independent of depth. We have estimated U_r as the depth-independent current in the deepest portion of the profiles. (Figure A1 is an example.) The estimated U_r were usually less than 0.1 m s^{-1}.

For most purposes we need to separate the currents from the wave orbital motions, and it is convenient to work with layer-averaged currents rather than an arbitrary current profile. To do this we have fitted the observed current profiles to a model composed of a single surface wave and a three-layer linear current profile, $L(z)$, where z is the vertical coordinate = 0 at the sea surface and positive upward. Thus, for the east component, we fit

$$U(z) = \exp^{kz}[a\cos(\omega z/W) + b\sin(\omega z/W)] + L(z), \quad (14)$$

where $k = \omega^2/g$ is the vertical wavenumber, ω is the wave frequency estimated from the observed wave os-

TABLE A2. Coefficients for three-layer model fit to Gloria AXCP profiles. In column one D is the AXCP number. Z_0 is the start of usable data (m). TML is the temperature of the surface mixed layer (C). P is the period of the surface wave (s), and a and b are the cosine and sine coefficients of the fit to the surface wave (cm s^{-1}). The first row of data for each AXCP is the east component, and the second row is the north component (all directions are true). Z_i is the depth of the bottom of layer i (m), U_i is the mean current in the layer (cm s^{-1}), and U_{zi} is the shear (cm s^{-1} m^{-1}). The reference velocity has been subtracted away. R is the rms difference between the observed and the best fit profile (cm s^{-1}). The format of this table exactly follows Tables 1 and 2 of Sanford et al. (1987), which give Norbert and Josephine data.

D#	Z_0/TML		P	a	b	Z_1	U_1	U_{Z1}	Z_2	U_2	U_{Z2}	Z_3	U_3	U_{Z3}	R
G5	0	U	11	65	−28	−33	105	0.40	−76	43	2.58	−200	−6	−0.11	4
	25.8	V	10	30	55	−33	88	1.15	−76	42	1.23	−200	15	0.01	5
G7	0	U	10	52	41	−40	118	0.96	−75	41	3.26	−200	−16	0.01	3
	25.8	V	10	57	−94	−40	71	0.03	−75	44	1.48	−200	17	0.02	9
G11	0	U	15	0	18	−51	−40	−0.68	−58	−20	−0.80	−200	−16	−0.01	6
	24.7	V	15	41	1	−51	81	1.17	−58	25	7.90	−200	−1	−0.02	7
G12	0	U	12	59	−64	−33	−72	−0.66	−69	−29	−1.79	−200	0	0.06	8
	26.1	V	12	2	85	−33	107	0.69	−69	53	2.35	−200	9	0.03	6
G13	0	U	10	−1	40	−44	−21	0.18	−78	−13	−0.71	−200	−2	0.01	3
	26.0	V	10	−61	−14	−44	−30	−0.13	−78	−19	−0.50	−200	−4	−0.09	6
G15	0	U	13	18	−27	−36	−31	0.02	−65	−9	−1.51	−200	7	0.09	6
	26.4	V	13	−5	−24	−36	−69	0.06	−65	−50	−1.37	−200	−18	−0.17	7
G16	0	U	13	39	−19	−50	−50	−0.41	−69	−40	0.03	−200	−29	−0.17	5
	25.7	V	13	−101	64	−50	58	0.96	−69	19	1.53	−200	1	0.05	6
G17	0	U	14	−36	89	−55	−54	−0.18	−73	−51	0.23	−200	−37	−0.24	4
	25.5	V	12	73	−90	−55	24	0.13	−73	4	1.88	−200	−4	−0.15	5
G18	0	U	12	113	−95	−40	−52	0.10	−55	−41	−1.70	−200	−22	−0.08	4
	25.6	V	13	−105	22	−40	29	0.48	−55	9	1.26	−200	4	−0.05	6
G19	−10	U	13	−213	−54	−75	−92	−1.30	−113	−43	−0.36	a	a	a	6
	27.2	V	13	189	33	−75	68	−0.02	−113	43	1.28	a	a	a	11
G21	0	U	12	−61	−34	−53	−57	0.26	−80	−35	−2.11	−200	−3	−0.07	7
	26.5	V	12	89	5	−53	41	−0.20	−80	36	0.79	−200	22	0.06	7
G24	0	U	13	51	15	−45	−84	−1.14	−65	−24	−3.47	−200	7	0.07	6
	26.5	V	12	46	−1	−45	39	−0.20	−65	25	1.83	−200	0	0.10	8
G25	0	U	9	−13	45	−58	97	−0.07	−84	65	2.58	−200	26	0.10	2
	26.5	V	9	136	−37	−58	132	1.56	−84	49	2.87	−200	5	0.13	3
G27	0	U	10	45	70	−55	40	0.51	−95	23	0.12	−200	17	0.08	4
	26.7	V	9	99	−8	−55	166	1.19	−95	79	2.72	−200	16	0.17	6
G31	0	U	11	46	−51	−57	−19	−1.17	−66	11	0.83	−200	5	0.03	3
	27.7	V	11	0	9	−57	1	−0.21	−66	4	0.74	−200	3	0.04	2

cillation and given the fall rate W, and g is the acceleration of gravity. The coefficients a, b are found by a least-squares fitting, and note that the surface amplitude of the wave is just $U_W = (a^2 + b^2)^{1/2}$; $L(z)$ is the current profile:

$$L(z) = U_1 + U_{Z1}(z - Z_1/2) \quad \text{if} \quad Z_0 \geq z \geq Z_1$$

$$L(z) = U_2 + U_{Z2}(z - (Z_1 + Z_2)/2) \text{ if } Z_1 \geq z \geq Z_2$$

$$L(z) = U_3 + U_{Z3}(z - (Z_2 + Z_3)/2) \text{ if } Z_2 \geq z \geq Z_3, \tag{15}$$

where Z_0 is the start of usable data, Z_i are the depths of the layers (Table A1), and U_i and U_{Zi} are the depth-averaged current and shear found by the fitting procedure. These are constrained to yield a continuous profile across the layer boundaries.

The layer depths were chosen subjectively based upon the observed structure of the temperature and current profiles, and with a definite physical model in mind. Layer 1 was taken to be a surface mixed layer within which the temperature was uniform to within 0.2°C, though the current may have a shear, U_{Z1}; layer 2 was taken to be the transition layer at the base of the mixed layer, which is strongly sheared and stratified; layer 3 was taken to be the upper thermocline. This three-layer model seemed apt for most of the profiles, and especially those with strong hurricane-driven currents. This can be judged in part by noting that the rms current that could not be accounted for by the fit,

TABLE A3. AXCP current data in the storm-centered coordinate system. In column one D is the AXCP number; N denotes Norbert; J, Josephine; G, Gloria. U_W and V_W are the across- and alongtrack amplitude of the wave component at the surface (direction is ambiguous to 180°). U_i and V_i are the across- and alongtrack currents averaged over layer i, and U_{zi}, V_{zi} are the corresponding shears. a: AXCP G19 did not go deep enough to measure layer 3.

	U_W	V_W	U_1	V_1	U_{Z1}	V_{Z1}	U_2	V_2	U_{Z2}	V_{Z2}	U_3	V_3	U_{Z3}	V_{Z3}
D	(cm s^{-1})		(cm s^{-1})		(cm s^{-1} m^{-1})		(cm s^{-1})		(cm s^{-1} m^{-1})		(cm s^{-1})		(cm s^{-1} m^{-1})	
N2	63.	18.	17.	16.	0.21	−0.03	11.	3.	0.03	1.06	2.	−6.	0.14	−0.07
N3	−84.	33.	−43.	−101.	−0.50	−0.48	−23.	−55.	−1.36	−4.30	−10.	−6.	−0.03	−0.14
N4	−91.	−132.	11.	21.	−0.19	−1.56	6.	21.	0.43	1.34	−1.	−7.	−0.01	0.07
N6	110.	221.	29.	73.	−0.53	1.41	23.	29.	1.83	3.02	4.	2.	0.08	0.06
N13	−80.	17.	80.	51.	−0.41	0.74	35.	8.	2.97	1.72	−18.	−15.	0.01	−0.12
N14	−10.	104.	80.	−3.	1.03	0.36	27.	−13.	3.12	0.34	−11.	−16.	−0.02	−0.01
N15	−23.	17.	−68.	73.	−0.50	0.65	−31.	33.	−2.40	2.53	0.	1.	−0.02	−0.01
N16	20.	42.	−10.	87.	1.09	0.69	−15.	30.	−1.15	3.55	1.	−6.	−0.02	−0.12
N18	−41.	134.	54.	−29.	3.31	−0.43	21.	−27.	−0.48	0.26	11.	−26.	0.51	−0.11
N20	30.	111.	21.	−105.	−0.09	−2.93	16.	−53.	0.46	−1.18	−3.	−18.	0.19	−0.30
N21	−126.	−43.	−18.	−99.	−0.19	−0.54	−4.	−65.	−0.57	−1.43	−2.	−23.	0.19	−0.47
N22	−34.	54.	59.	−26.	1.19	−0.15	25.	−21.	2.06	−0.41	3.	−5.	0.13	−0.25
N23	17.	90.	77.	−33.	3.19	−1.41	18.	−17.	−1.45	0.71	1.	−6.	0.13	−0.32
N24	−7.	81.	43.	−33.	1.37	0.39	5.	−39.	1.87	−0.23	−16.	−21.	0.14	−0.30
N26	−190.	86.	−13.	0.	−1.98	−0.20	11.	7.	−0.18	−0.41	3.	4.	0.14	0.09
N31	63.	53.	−65.	21.	−5.08	−0.29	15.	16.	−0.31	0.93	8.	−1.	0.12	0.10
J2	−9.	−69.	11.	15.	0.07	0.02	9.	9.	0.08	0.94	4.	1.	0.07	0.05
J3	1.	59.	6.	43.	−0.03	−0.14	15.	38.	−1.52	2.08	16.	20.	0.13	0.15
J4	76.	−28.	−3.	24.	0.75	−0.63	−16.	18.	−0.76	4.22	−11.	1.	−0.03	−0.05
J7	−73.	22.	9.	43.	−0.18	0.45	11.	2.	0.76	3.18	5.	−14.	0.00	−0.13
J8	38.	−3.	30.	16.	0.26	0.10	5.	5.	2.69	1.30	−7.	−3.	−0.11	−0.02
J13	−122.	10.	36.	21.	−1.75	−0.27	43.	17.	3.76	1.19	14.	7.	0.01	0.03
J14	14.	−43.	33.	29.	0.07	0.49	16.	8.	2.12	1.06	2.	0.	−0.03	0.01
J17	−22.	−40.	44.	58.	0.06	0.46	30.	11.	1.28	3.05	14.	−15.	0.05	−0.09
J20	−25.	20.	−8.	25.	−0.07	0.28	−13.	7.	0.91	1.25	−16.	0.	−0.06	−0.03
J21	18.	50.	−3.	15.	0.34	−0.78	−8.	10.	−0.33	4.31	−5.	−7.	−0.02	−0.06
J25	12.	73.	20.	12.	0.35	0.25	6.	16.	1.03	−3.21	−2.	19.	0.07	0.12
J26	24.	50.	4.	−2.	−0.01	0.15	−4.	−1.	1.55	−0.96	−9.	−1.	−0.04	0.06
J27	137.	−29.	−1.	15.	0.18	0.01	−11.	11.	0.84	0.61	−13.	5.	−0.03	0.04
J29	−18.	−13.	−1.	−14.	1.11	1.86	−15.	−12.	−0.16	−2.99	−10.	20.	−0.05	−0.04
G5	95.	25.	137.	10.	1.00	0.69	59.	9.	2.81	−0.52	4.	16.	−0.08	0.08
G7	111.	69.	137.	−12.	0.80	−0.54	59.	11.	3.50	−0.72	−3.	23.	0.02	0.01
G11	34.	26.	16.	89.	0.14	1.34	−1.	31.	4.00	6.86	−14.	8.	−0.02	−0.01
G12	114.	44.	5.	129.	−0.13	0.95	8.	59.	−0.06	2.95	5.	7.	0.06	−0.01
G13	−67.	−43.	−35.	−12.	0.07	−0.21	−22.	−7.	−0.87	0.01	−5.	−2.	−0.04	−0.08
G15	22.	−32.	−65.	−38.	0.05	0.04	−37.	−35.	−2.03	−0.22	−5.	−19.	−0.02	−0.19
G16	−33.	−119.	−6.	76.	0.24	1.02	−21.	39.	0.92	1.22	−23.	18.	−0.11	0.14
G17	−15.	144.	−30.	51.	−0.07	0.21	−39.	33.	1.29	1.39	−32.	18.	−0.28	0.02
G18	73.	−151.	−25.	54.	0.37	0.33	−27.	32.	−0.64	2.02	−15.	16.	−0.10	0.01
G19	−76.	269.	−35.	109.	−1.06	0.75	−10.	61.	0.46	1.25	a	a	a	a
G21	−7.	112.	−22.	67.	0.10	−0.31	−7.	50.	−1.24	1.88	10.	19.	−0.02	0.09
G24	73.	11.	−45.	81.	−1.04	0.51	−5.	34.	−1.73	3.51	6.	−4.	0.11	0.04
G25	105.	127.	156.	50.	0.86	1.30	81.	2.	3.77	0.80	23.	−11.	0.16	0.04
G27	122.	39.	130.	111.	1.11	0.67	65.	50.	1.70	2.13	23.	3.	0.16	0.09
G31	68.	−17.	−15.	12.	−1.07	0.52	11.	−3.	1.11	0.11	5.	−1.	0.00	−0.04

R, was typically less than 0.1 m s^{-1}. The three-layer model coefficients for Gloria are listed in Table 2A; S87 gives the same from Norbert and Josephine. Currents in the storm-centered coordinate system are listed in Table A3.

REFERENCES

Archer, D. A., 1990: Modeling pCO2 in the upper ocean: A review of relevant physical, chemical and biological processes. TRO50, University of Washington, Seattle, 61 pp.

Black, P. G., 1983: Ocean temperature changes induced by tropical cyclones. Ph.D. thesis, The Pennsylvania State University, 278 pp.

——, R. L. Elsberry, L. K. Shay, R. Partridge, and J. Hawkins, 1988: Hurricane Josephine surface winds and ocean response determined from air-deployed drifting buoys and concurrent research aircraft data. *J. Atmos. Oceanic Technol.*, **5**, 683–698.

Brink, K. H., 1989: Observations of the response of thermocline currents to a hurricane. *J. Phys. Oceanogr.*, **19**, 1017–1022.

Brooks, D., 1983: The wake of hurricane Allen in the western Gulf of Mexico. *J. Phys. Oceanogr.*, **13**, 117–129.

Cardone, V. J., and D. B. Ross, 1979: State-of-the-art wave prediction methods and data requirements. *Ocean Wave Climate,* M. D. Earle and A. Malahoff, Eds., Plenum Publishing Corp., 61–91.

——, A. J. Broccoli, C. V. Greenwood, and J. A. Greenwood, 1980: Error characteristics of extratropical storm wind fields specified from historical data. *J. Petrol. Technol.,* **32,** 873–880.

Chang, S. W., and R. A. Anthes, 1978: Numerical simulations of the ocean's nonlinear, baroclinic response to translating hurricanes. *J. Phys. Oceanogr.,* **8,** 468–480.

Church, J. A., T. M. Joyce, and J. F. Price, 1989: Current and density observation across the wake of Hurricane Gay. *J. Phys. Oceanogr.,* **19,** 259–265.

Cooper, C., and J. D. Thompson, 1989a: Hurricane-generated currents on the outer continental shelf Part 1: Model formulation and verification. *J. Geophys. Res.,* **94,** 12 513–12 539.

——, and ——, 1989b: Hurricane-generated currents on the outer continental shelf Part 2: Model sensitivity studies. *J. Geophys. Res.,* **94,** 12 540–12 554.

Cornillon, P., L. Stramma, and J. F. Price, 1987: Satellite measurements of sea surface cooling during hurricane Gloria. *Nature,* **326,** 373–375.

D'Asaro, E. D., 1989: The decay of wind-forced mixed layer inertial oscillations due to the β effect. *J. Geophys. Res.,* **94,** 2045–2056.

Emanuel, K. A., 1988: Toward a general theory of hurricanes. *Am. Sci.,* **76,** 370–379.

Forristall, G. Z., R. C. Hamilton, and V. J. Cardone, 1977: Continental shelf currents in Tropical Storm Delia: Observation and theory. *J. Phys. Oceanogr.,* **7,** 532–546.

——, E. G. Ward, V. J. Cardone, and L. E. Borgman, 1978: The directional spectra and kinematics of gravity waves in Tropical Storm Delia. *J. Phys. Oceanogr.,* **8,** 888–909.

——, R. D. Larrabee, and R. S. Mercier, 1991: Combined oceanographic criteria for deep water structures in the Gulf of Mexico. *The 23rd Offshore Technology Conf.,* Paper OTC6541, 377–390.

Frank, W. M., 1977: The structure and energetics of the tropical cyclone I. Storm structure. *Mon. Wea. Rev.,* **105,** 1119–1135.

Geisler, J. E., 1970: Linear theory of the response of a two-layer ocean to a moving hurricane. *Geophys. Fluid Dyn.,* **1,** 249–272.

Gill, A. E., 1984: On the behavior of internal waves in the wakes of storms. *J. Phys. Oceanogr.,* **14,** 1129–1151.

Ginis, I., and K. Z. Dikiniov, 1989: Modeling the effect of typhoon Virginia (1978) on the ocean. *Sov. Meteorol. Hydrol.,* **7,** 53–60.

Greatbatch, R. J., 1983: On the response of the ocean to a moving storm: The nonlinear dynamics. *J. Phys. Oceanogr.,* **13,** 357–367.

——, 1984: On the response of the ocean to a moving storm: parameters and scales. *J. Phys. Oceanogr.,* **14,** 59–78.

——, 1985: On the role played by upwelling of water in lowering sea surface temperatures during the passage of a storm. *J. Geophys. Res.,* **90,** 11 751–11 755.

Klein, P., and B. L. Hua, 1988: Mesoscale heterogeneity of the wind-driven mixed layer: Influence of a quasigeostrophic flow. *J. Mar. Res.,* **46,** 495–525.

Large, W. G., and S. Pond, 1981: Open ocean momentum flux measurements in moderate to strong winds. *J. Phys. Oceanogr.,* **11,** 324–336.

——, J. C. McWilliams, and P. P. Niiler, 1986: Upper ocean thermal response to strong autumnal forcing of the Northeast Pacific. *J. Phys. Oceanogr.,* **16,** 1524–1550.

Malkus, J., 1962: Large scale interactions. *The Sea, Vol. I,* M. N. Hill, Ed., Interscience, 88–294.

Martin, P. J., 1982: Mixed-layer simulation of buoy observations taken during Hurricane Eloise. *J. Geophys. Res.,* **87,** 409–427.

——, 1986: Testing and comparison of several mixed-layer models, TR-143. Naval Ocean Research and Development Activity, NSTL, MS, 31 pp.

Mellor, G. L., and T. Yamada, 1982: Development of a turbulence closure model for geophysical fluid problems. *Rev. Geophys. Space Phys.,* **20,** 851–875.

Miller, B. J., 1964: A study of the filling of Hurricane Donna (1960) over land. *Mon. Wea. Rev.,* **92,** 389–406.

NOAA NWS, 1979: Meteorological criteria for standard project hurricane and probable maximum hurricane wind fields, Gulf of Mexico and east coast of the United States. NOAA Tech. Rep. NWS 23, U.S. Department of Commerce, Washington D.C., 320 pp.

Powell, M. D., 1980: Evaluations of diagnostic marine boundary layer models applied to hurricanes. *Mon. Wea. Rev.,* **108,** 757–766.

Price, J. F., 1981: Upper ocean response to a hurricane. *J. Phys. Oceanogr.,* **11,** 153–175.

——, 1983: Internal wave wake of a moving storm. Part I: Scales, energy budget and observations. *J. Phys. Oceanogr.,* **13,** 949–965.

——, R. A. Weller, and R. Pinkel, 1986: Diurnal cycling: Observations and models of the upper ocean response to diurnal heating, cooling, and wind mixing. *J. Geophys. Res.,* **91,** 8411–8427.

——, T. B. Sanford, and G. Z. Forristall, 1991: Ocean response to a hurricane. Part II: Data tabulations and numerical modeling. Woods Hole Oceanographic Institution Tech. Rep. WHOI-91-6, 71 pp.

Sanford, T. B., P. G. Black, J. R. Haustein, J. W. Feeney, G. Z. Forristall, and J. F. Price, 1987: Ocean response to a hurricane, Part I: Observations. *J. Phys. Oceanogr.,* **17,** 2065–2083.

Shay, L. K., and R. L. Elsberry, 1987: Near-inertial ocean current response to hurricane Frederick. *J. Phys. Oceanogr.,* **17,** 1249–1269.

——, ——, and P. G. Black, 1989: Vertical structure of the ocean current response to a hurricane. *J. Phys. Oceanogr.,* **19,** 649–669.

Stewart, R. W., 1974: The air–sea momentum exchange. *Bound.-Layer Meteor.,* **6,** 151–167.

Stramma, L., P. Cornillon, and J. F. Price, 1986: Satellite observations of sea surface cooling by hurricanes. *J. Geophys. Res.,* **91,** 5031–5035.

Trowbridge, J. H., 1992: On a simple representation of mixing in a stress-driven stratified flow. *J. Geophys. Res.,* **97,** 15 529–15 544.

Voorhis, A. D., 1969: The horizontal extent and persistence of thermal fronts in the Sargasso Sea. *Deep Sea Res.,* **16**(Suppl.), 331–337.

Willmott, C. J., S. G. Ackelson, R. E. Davis, J. J. Feddema, K. M. Klink, D. R. Legates, J. O'Donnell, and C. M. Rowe, 1985: Statistics for the evaluation and comparison of models. *J. Geophys. Res.,* **91,** 8995–9005.